Transformed notochordal cells trigger chronic wounds destabilizing the vertebral column and bone homeostasis

Authors: Paco López-Cuevas[1], Luke Deane[1], Yushi Yang[2, 3, 4], Chrissy L Hammond[5] and Erika Kague[5]*

Affiliations:

[1]The School of Biochemistry, Biomedical Sciences, University of Bristol, BS8 1TD, UK.

[2]School of Physics, HH Wills Physics Laboratory, University of Bristol, BS8 1TL, UK.

[3]Centre for Nanoscience and Quantum Information, University of Bristol, Bristol, BS8 1FD, UK.

[4] Bristol Centre for Functional Nanomaterials, University of Bristol, Bristol, BS8 1TL, UK.

[5]The School of Physiology, Pharmacology and Neuroscience, Biomedical Sciences, University of Bristol, BS8 1TD, UK.

*Correspondence to: erika.kague@bristol.ac.uk

Summary statement

Zebrafish chordomas resemble unhealed wounds. They compromise the notochord structure, causing chronic inflammation, impairing intervertebral discs patterning and bone homeostasis. By controlling inflammation one can control chordoma development.

Keywords

Chordoma, notochord, vertebral column, zebrafish intervertebral disc, inflammation, bone homeostasis

Abstract

Notochordal cells play a pivotal role in vertebral column patterning, contributing to the formation of the inner architecture of intervertebral discs (IVDs). Their disappearance during development has been associated with reduced repair capacity and IVD degeneration. Notochordal remnants are known to cause chordomas, a highly invasive bone cancer associated with late diagnosis. Understanding the impact of neoplastic cells during development and on the surrounding vertebral column could open avenues for earlier intervention and therapeutics. We investigated the impact of transformed notochord cells in the zebrafish skeleton using a RAS expressing line in the notochord under the control of the *Kita* promoter, with the advantage of adulthood endurance. Transformed cells caused damage in the notochord and destabilised the sheath layer triggering a wound repair mechanism, with enrolment of sheath cells (*col9a2*+) and expression of *wt1b,* similar to induced notochord wounds. Moreover, increased recruitment of neutrophils and macrophages, displaying abnormal behaviour in proximity to the notochord sheath and transformed cells, supported parallels between chordomas, wound and inflammation. Cancerous notochordal cells interfere with differentiation of sheath cells to form chordacentra domains leading to fusions and vertebral clefts during development. Adults displayed IVD irregularities reminiscent of degeneration; reduced bone mineral density, increased osteoclast activity; while disorganised osteoblasts and collagen indicate impaired bone homeostasis. By depleting inflammatory cells, we abrogated chordoma development and rescued the skeletal features of the vertebral column. Therefore, we showed that transformed notochord cells alter the skeleton during life, causing a wound-like phenotype and activating chronic wound response, suggesting parallels between chordoma, wound, IVD degeneration and inflammation, highlighting inflammation as a promising target for future therapeutics.

Introduction

The vertebral column is the central axis of the skeleton in all vertebrates. It is composed of segments (vertebrae) connected by joint-like structures called intervertebral discs (IVDs). In mammals, the architecture of the IVDs is made by an annulus fibrosus (AF), a collagenous layer surrounding a hydrated and gelatinous nucleus pulposus (NP) core, which contains chondrocyte-like cells derived from embryonic notochord cells (Rodrigues-Pinto et al., 2014). The disappearance of notochordal cells in mammals during development of the vertebral column has been linked to reduction of repair capacity and IVD degeneration (IVDD) (Wang et al., 2017). Occasionally, notochordal remnants are observed (Yamaguchi et al., 2004), causing vertebral malformations and in rare cases cell transformation lead to chordomas (Salisbury, 1993, Choi et al., 2008), a rare bone cancer of the axial skeleton and skull base (McMaster et al., 2011).

With an incidence of approximately one in a million, chordomas account for about 1-4% percent of all primary bone malignancies and 20% of primary spinal tumours (Chugh et al., 2007). Chordomas are slow growing and highly resistant to both chemotherapy and radiotherapy, meaning that radical surgery is often the primary choice for treatment modality (McMaster et al., 2011). Unfortunately, in many cases, the proximity of chordomas to vital structures, means that local excision is rarely achieved, resulting in a recurrence rate greater than 50% (Stacchiotti et al., 2017, Barry et al., 2011). Distant metastases to lung, bone, soft tissue, lymph node, liver, and skin have been reported in up to 43% of cases (Stacchiotti et al., 2017, Barry et al., 2011). Interestingly, chordomas lead to changes in bone quality, and often appear on X-rays and computerised tomography (CT) as eroding bone lesions with associated soft tissue calcification (de Bruine and Kroon, 1988), suggesting modifications in the behaviour of the nucleus pulposus cells disrupt disc and bone homeostasis. Impairment of disc homeostasis is a hallmark of IVDD (Novais et al., 2020a), which unlike chordomas is

very common, representing the most common cause of back pain (Zheng and Chen, 2015), a symptom that 80% of the adult world population suffer from (GBD et al., 2017). How transformed nucleus pulposus cells affect the IVD and surrounding vertebrae during their development is currently unknown; and no animal models to show how transformed cells dynamically interact with and affect the IVDs and vertebral column *in vivo* have been described. Such models could contribute to our understanding of chordoma development, IVDD, the interaction of the nucleus pulposus with the skeletal tissues and feature possible therapeutic avenues for both conditions.

Zebrafish have emerged as an advantageous animal model for a variety of human diseases, including cancer and skeletal diseases, due to their fast development, tractability, flexible genetic manipulation (transgenesis, forward and reverse genetics) and their translucency (Bergen et al., 2019). Reporter lines allow *in vivo* assessment of cell behaviour not only during early development but also during the later stages of skeletal formation in juveniles (Bergen et al., 2019). Zebrafish have high tissue regenerative capacity, with the ability to restore vacuolated cells of the notochord upon injury (Garcia et al., 2017). In zebrafish, notochord cells remain throughout life; they are enveloped by a sheath layer that acts as a sealing basement membrane to isolate the inner notochord vacuolated cells, and carries high potential to mineralise (Fleming et al., 2004, Stemple, 2005). The notochord sheath plays an important role in the segmentation of the vertebral column and centra primordium (chordacentra) formation (Lleras Forero et al., 2018, Pogoda et al., 2018, Wopat et al., 2018). Following genetic manipulation, mechanical injury (needle punctures) or chemical treatment (with nystatin), repair of tissue damage appears to involve a sub-population of notochord sheath cells which become activated, expressing Wilms Tumor 1 (*wt1b*), and migrate towards the wound, setting landmarks during notochord repair (Garcia et al., 2017, Lopez-Baez et al., 2018).

Chordoma onset has been described in larval zebrafish expressing the oncogene *RAS* in the notochord, using the bimodal Gal4/UAS system and activation of the oncogenic RTK/Ras pathway (Burger et al., 2014). These zebrafish chordoma models become affected within the first 3 days post-fertilisation (dpf), progressively developing notochord hyperplasia , similar to histological features of human chordomas (Burger et al., 2014). Recently, the zebrafish chordoma model was used to test genetic potential to transform the notochord *in vivo*, providing suggestive evidence that Brachyury (*TBXT*), a highly expressed gene in human chordomas (Vujovic et al., 2006), is insufficient to initiate chordomas, instead suggesting activation of members of the RTK signalling as potential players in chordoma formation (D'Agati et al., 2019). The behaviour of notochord cancer cells during zebrafish life has not yet been studied, due to early lethality of chordoma models during larval stages. It is unknown whether notochord cancer cells trigger a wound repair mechanism similar to those of notochord injury models, which activate an acute inflammatory response as is seen in other early cancers (Feng et al., 2012, Feng et al., 2010). It is also unclear whether notochord cancer cells exert control as notochordal remnants to interfere with bone formation and, later in life, with bone homeostasis.

Here we studied the interactions between the notochord cancer cells within the forming vertebral column and bone homeostasis using a well-characterised transgenic line, *Kita-RAS*, which drives expression of HRASV12 in the notochord (and in melanoblasts, thus modelling melanoma) and survives to adulthood (Santoriello et al., 2010, van den Berg et al., 2019, Feng et al., 2012). We showed that “transformed” notochord cells destabilise the notochord sheath layer, activating a chronic wound repair response similar as those caused by induced notochord wounds previously described (Garcia et al., 2017, Lopez-Baez et al., 2018). These pre-neoplastic cells lead to invagination of the *col9* expressing notochord sheath cells towards the wound and participation of *wt1b* notochord sheath sub-population.

Interestingly, macrophages and neutrophils were present in higher numbers and showed prolonged interaction with the wounded notochord sheath layer, as described in other cancers. The metameric pattern of segmentation of the vertebral column was compromised, but not abrogated, leading to vertebral fusions and clefts. Adult bone homeostasis was altered as observed by differences in vertebral bone mineral density and collagen fibre distribution. Transformed cells also compromised the adult zebrafish equivalent intervertebral disc architecture, leading to NP "scar" tissue, NP cellular disorganisation and affecting the structure of the AF, similar to IVDD. Chordoma development and skeletal defects were rescued when we partially depleted neutrophils and macrophages. In conclusion, our results indicate that transformed notochord cells cause chronic wounds leading to inflammation, vertebral abnormalities, disc and bone homeostasis impairment. Chordoma development could be controlled by limiting inflammation, revealing new avenues for therapeutics and highlighting the use of zebrafish as an animal model.

Results

Kita-RAS induces wound-like destabilisation of the notochord

Notochord-specific *Gal4* lines crossed to *UAS:EGFP-HRASV12* have been previously described as powerful models for inducing chordomas in zebrafish (Burger et al., 2014). A transgenic line extensively used to induce melanoma, in which *HRASV12* expression is driven by the *Kita* promoter in melanoblasts, goblet cells and in the notochord cells has the advantage over other notochord RAS expressing lines because it survives to adulthood (Santoriello et al., 2010, van den Berg et al., 2019). We used *Kita-RAS-GFP* and *Kita-RAS-mCherry* to study the progressive changes of the transformed notochord cells and their interaction with the forming vertebral column. In 5dpf zebrafish larvae, the outer layer of the notochord is formed by an epithelial-like sheath wrapping notochord vacuolated cells (Wopat et al., 2018) (Fig. 1A). Confocal images through the notochord, at 5dpf, showed that *Kita* drives reporter expression in the notochord vacuolated cells, but not in the sheath cells (Fig. 1B). As in other chordoma RAS models, *Kita-RAS* led to dramatic destabilisation of the notochord vacuolated cells starting as early as 3dpf and by 5dpf affected 70% of the larvae (>200 larvae analysed). Affected larvae were considered when they displayed more than 3 lesions in the notochord. Each lesion was characterised by increased RAS expression and abnormal notochord cell morphology (Fig. 1B). At the same developmental stage (5dpf), notochord cells were interspaced by infiltration of non-vacuolated cells and accumulation of fibrous collagenous tissue (AFOG staining, red colour) (Fig. 1B-C). Furthermore, histological sections suggested local destabilisation of the notochord sheath layer at the region of collapsed vacuolated cells (Fig. 1C). To analyse cell proliferation, we treated larvae with EdU solution to be incorporated into the DNA of proliferating cells from 2 to 4dpf and followed by counting the number of EdU-positive (+) cells at 5dpf from confocal images. Notochord cells and notochord sheath cells in *Kita-RAS* are highly proliferative (p= 0.0002)

(Fig. 1D and E). Interestingly, the organisation of the notochord in *Kita-RAS* fish displayed cellular characteristics reminiscent of those observed in notochord wounding models (needle puncture)(Lopez-Baez et al., 2018) (Fig. S1), suggesting that chordoma may recapitulate repair mechanisms, as has been suggested for several other cancers (Feng et al., 2010).

Pre-neoplastic notochord cells trigger the notochord wound repair mechanism in zebrafish

Wounds in the notochord induced by needle injury, amputation and chemical damage lead to the collapse of notochord vacuolated cells, sheath cell invasion and expression of Wilms Tumor 1b (*wt1b*) within a cell sub-population of the notochord sheath (Garcia et al., 2017, Lopez-Baez et al., 2018). To investigate whether pre-neoplastic notochord cells mimic a wound-like response, we crossed *Kita-RAS-mCherry* with Tg(*col9a2:GFPCaaX*), a marker for the notochord sheath layer (Fig. 2A), and to Tg(*wt1b:gfp*) to label the sub-population of sheath cells that standardly respond to damage. We confirmed that at 5dpf *Kita* is not expressed in the notochord sheath layer, and only in the notochord cells (Fig. 2B). We observed *col9a2* expression in regions of damage within the notochord, suggesting sheath cell migration towards the chordoma wounded area (Fig. 2B). Cross sections through the notochord, at 5dpf, showed *col9a2* expressing cells within the notochord in connection with the notochord sheath (Fig. 2B), reinforcing the possible migration of sheath cells to the lesioned region. To check for cell abnormalities in the notochord sheath, we quantified the cell area of the *col9+* cells within two regions of our *Kita-RAS*, wound- proximal and distal (Fig. 2C). *Kita-RAS* showed significant reduction in cell area in wound-proximal regions ($p < 0.0001$), but not in wound-distal regions when compared to controls (Fig. 2C). Therefore, wound-like lesions caused by transformed notochord cells lead to local cellular modifications in the sheath layer. Next, we analysed *wt1b* expression in the *Kita-RAS* outcrossed fish. Control fish exhibited no expression of *wt1b* in the notochord, whereas *Kita-RAS* showed

strong *wt1b* expression by pre-neoplastic cells located at severe wounded regions in 100% of the cases analysed (20/20) (Fig. 2E). These findings corroborate strong parallels between cancer and wound repair (MacCarthy-Morrogh and Martin, 2020).

Wounded notochord sheath elicits a prolonged recruitment of innate inflammatory cells

Several studies have reported that oncogene-transformed cells trigger an innate inflammatory response, with both neutrophils and macrophages recruited to the pre-cancerous tissue (Chia et al., 2018, Feng et al., 2010, Freisinger and Huttenlocher, 2014, Roh-Johnson et al., 2017). This recruitment of neutrophils and macrophages is responsible for clearing cell debris and to orchestrate tissue repair responses including wound angiogenesis and matrix deposition (Eming et al., 2017). We questioned whether oncogenic RAS expression in the notochord cells and the lesioned notochord sheath might also induce an inflammatory response in our zebrafish chordoma model. During the first weeks of development, zebrafish do not have a functional adaptive immune system, allowing us to investigate the innate immune response on its own (Renshaw and Trede, 2012). We performed time-lapse imaging at 5dpf and analysed the interactions of neutrophils and macrophages with the notochord sheath layer. For neutrophils, we incrossed Tg(*kita:Gal4; UAS:mCherry; UAS:HRASG12V-GFP;lyz:DsRed*), and selected RAS-/lyz+ larvae, Tg(*kita:mCherry;lyz:DsRed*), and RAS+/lyz+ larvae, Tg(*kita:HRASG12V-GFP;lyz:DsRed*), as controls and *Kita-RAS* fish, respectively. While for macrophages, we incrossed Tg(*kita:Gal4;UAS:mCherry;UAS:HRASG12V-GFP;mpeg:FRET*), selected RAS-/mpeg+ larvae, Tg(*kita:mCherry;mpeg:FRET*) and RAS+/mpeg+ larvae, Tg(*kita:HRASG12V-GFP;mpeg:FRET*), as controls and *Kita-RAS* fish, respectively. Higher numbers of neutrophils and macrophages were recruited, making a prolonged direct contact with the wounded notochord sheath in *Kita-RAS* in comparison with controls (Fig. 3, Fig. S2 and Movies 1 and 2), similarly to the inflammatory response previously reported in the melanoma

model (Feng et al., 2010). Remarkably, we also found neutrophils and macrophages infiltrating wounded regions and in direct contact with notochord vacuolated cells (Fig. S2 and Movies 1 and 2). Together our results showed that zebrafish chordoma induces a chronic notochord inflammatory wound response with typical wound recruitment of neutrophils and macrophages. Inflammatory cells trespass the notochord sheath layer in wounded regions to form direct contact with transformed notochord cells, a similar behaviour described for other cancers (Feng et al., 2012).

Depletion of neutrophils and macrophages abolishes chordoma development

To further test whether the increased innate inflammatory response triggers the proliferation of neoplastic cells leading to wounds in the notochord, we transiently delayed innate immune cell development by injecting *pu.1* and *gcsfr* morpholinos (MO) (double knockdown), at the one cell stage embryos generated by incrosses of *Kita-RAS-GFP* fish (Fig. S3). Combined *pu.1* and *gcsfr* MO injections are used to transiently arrest myeloid lineage development in larval zebrafish until at least 4dpf, therefore generating larvae lacking neutrophils and macrophages (Feng et al., 2012, Liongue et al., 2009, Rhodes et al., 2005). We confirmed the efficiency of our morpholino experiment by injecting fish carrying labelled neutrophils and macrophages at 3dpf (Tg(*lyz:DsRed*;*mpeg:FRET*))(Fig. S3B). Blocking the development of inflammatory cells in *Kita-RAS* resulted in a reduction of larvae exhibiting wounded (> 5 lesions) notochordal phenotype from 44.37 % (control MO) to 8.56 % (*pu.1* + *gcsfr* MO) ($p < 0.0001$) at 3dpf (Fig. S3C and D). In addition, fish with affected notochord (8.56%) in the *pu.1* + *gcsfr* MO group showed a less severe (≤ 5 lesions) phenotype in comparison to the control MO group, suggesting that incomplete ablation of inflammatory cells can ameliorate chordoma. To complement our morpholino experiment, we used CRISPR/Cas9 system to target *pu.1* and *gcsfr* simultaneously. We were able to cause mutations with an efficiency rate

of 80%, validated by fragment length analysis, for each individual genes, at 5dpf. We analysed *Kita-RAS* larvae from morpholinos (MO) and CRISPR injections side-by-side at 5dpf (Fig. 4A). CRISPR injections led to a significant reduction in numbers of neutrophils ($p= 0.0012$) and macrophages ($p= 0.0478$), but this reduction was not as pronounced as that observed from MO injections ($p<0.0001$) (Fig. 4B-D). Morpholinos also led to a significant reduction in proliferation of notochord and notochord epithelium cells in *Kita-RAS* (Fig. 4E and F). While CRISPR injections reduced cell proliferation, they did not show statistical difference from *Kita-RAS* ($p= 0.2422$)(Fig. 4E and F). In comparison with non-affected notochords from controls, fluorescent stereomicroscopy pictures from *Kita-RAS* wounded notochords displayed different profiles of average pixel intensity. Notochordal lesions are detected by increased pixel intensity and enlargement of peak areas (Fig. 4G). This unbiased method allowed us to quantify the severity of notochordal wounds among the studied groups and to analyse whether we could rescue the affected notochordal phenotype upon MO and CRISPR injections. We compared *Kita* (control), *Kita-RAS* and *Kita-RAS* injected with either MO or CRISPRs. Similar to our cell proliferation experiment, we detected a partial notochordal rescue with CRISPR injections and significant rescue with MO (Fig. 4H). Therefore, we have shown that the increase in neutrophils and macrophages contribute to proliferation of cancer cells in the notochord and modulation of inflammatory cells could prevent clonal expansion and chordoma development, similar to what has been previously shown for melanomas (Feng et al., 2012).

Abnormal pattern of vertebral segmentation and mineralisation in *Kita-RAS* fish

It has been demonstrated that notochord damage can lead to defective patterning of the vertebral column (Lopez-Baez et al., 2018, Fleming et al., 2004, Nguyen-Chi et al., 2014). Given that *Kita-RAS* cause cellular changes and a wound-like response in the notochord we

questioned whether these events might have a downstream impact in the vertebral column segmentation. We crossed *Kita-RAS* to Tg(*entpd5:kaeda*), an early marker of the notochord segmentation and biomineralizing activity. Entpd5 hydrolyses nucleoside triphosphates, providing local inorganic monophosphate for biomineralization (Dallas and Bonewald, 2010, Huitema et al., 2012). During development of the vertebral column, *entpd5* is expressed in alternating segments of the sheath, which will form the mineralised chordacentra; while the interdomains will develop into intervertebral discs (IVDs) (Fig. 5A and D) (Wopat et al., 2018). We analysed larvae at 8dpf, at a stage when segmentation has started but is not yet finalised. A delay in chordacentra formation was observed in *Kita-RAS*, compared to control of similar range of length (3.8 to 4.1 mm) (Fig. 5B). Regions in which the notochord cells were compromised in *Kita-RAS* coincided with mis-patterning and ectopic expression of *entpd5:kaeda* (Fig. 5C). Expansion of the domain of each segment was observed ectopically in the future IVD area. These results indicate that cellular abnormalities of the notochord sheath compromise the differentiation of *col9+* sheath cells towards expression of *entpd5* in predetermined chordacentra domains during segmentation. Moreover, our findings suggest a role of the sheath layer and notochordal cells in domain specification. A major advantage of our *Kita-RAS* model in comparison with other notochord induced RAS models (Burger et al., 2014, D'Agati et al., 2019, Distel et al., 2009) is the fish survival to adult stages, beyond the stages of development that have been previously reported. This allowed us to study the effect of pre-neoplastic cells on the skeletal formation and homeostasis. To check for abnormalities in mineralized vertebral column segments, we used *in vivo* and *ex vivo* Alizarin Red S staining in 14dpf fish. We detected abnormal and uneven mineralization of the chordacentra along the whole notochord, compromising length and shape of the segments and the future IVD domains (Fig. 5E-G). We measured the length of the first seven mineralised vertebral segments from fish displaying similar sizes ($5 \leq$ fish length < 6 mm) (Fig. 5G). *Kita-RAS*

297 showed high variability and overall reduced length of segments (Fig. 5E). Our results
298 indicate that the presence of notochord cancer cells leads to a wounded notochord sheath
299 which modifies vertebral column segmentation pattern through ectopic activation of *entpd5*
300 and subsequent mineralization, which ultimately may cause vertebral fusions.

301 **Transformed notochord cells lead to vertebral column fusions and clefts**

302 Next, we sought to investigate the impact of pre-neoplastic cells in the vertebral column
303 architecture. For that, we analysed the adult vertebral column, looking for resulting bone
304 abnormalities. We used Alizarin Red staining (controls n = 10; *Kita-RAS* n = 10; 6 months
305 post-fertilisation - 6mpf), X-rays (controls n = 40; *Kita-RAS* n = 78; 1 year old fish) and
306 micro-computerised tomography (μCT) (controls n = 5; *Kita-RAS* n = 5; 6mpf) to compare
307 *Kita-RAS* with control fish of the same age. Vertebrae fusions were found in 100% of *Kita-*
308 *RAS* and in 0% of controls (controls n = 40; *Kita-RAS* n = 78) (Fig. 6 and Fig. S4). Fusions
309 involved two or more vertebrae along the vertebral column leading to shortening of the total
310 fish length. Those fish with most fusions had the most reduced lengths (Fig. 6A, E and Fig.
311 S4). The ribs were the most severely affected region of the vertebral column. We calculated
312 the length of six consecutive mineralised segments of the vertebral column, separated by
313 well-defined IVDs (Fig. 6A, dashed region). Besides uncovering increased length of
314 segments due to vertebral fusions ($p= 0.0411$), it highlighted high variability within the same
315 vertebral column region of *Kita-RAS* fish, demonstrating that there was no common
316 developmental pattern of fusions (Fig. 6C and D). Analysis of fish length from X-ray images
317 reinforced the length reduction observed in *Kita-RAS* ($p< 0.0001$) (Fig. 6E and F). *Kita-RAS*
318 also displayed shape abnormalities of vertebrae and arches, including enlarged regions,
319 broadening of arches and ectopic bone growth (Fig. S4). Enlarged areas were found in 40%
320 of *Kita-RAS* (Fig. S4B). Ectopic bone growth can be better visualised with higher resolution
321 μCT (5μm) (Fig. 6G) and Alizarin Red staining (Fig. S4C). Clefts through the centra and

hemicentrae were found in 70% of fish analysed. These resembled butterfly abnormalities as occasionally described in human vertebral columns (Katsuura and Kim, 2019), and those malformations involving notochordal remnants (Fig. 6G’’’) (Oner et al., 2006). When staining 1 month old (1mpf) *Kita-RAS* with Alizarin Red, we detected hyperplastic cells contributing to a chaotic notochord cell arrangement along the vertebral column, and failure to organise in IVDs domains, revealing regions of incomplete mineralisation, originating clefts (Fig. 6H). To visualise osteoblasts, we crossed *Kita-RAS* fish to Tg(*osx:NTR-mCherry*), an osteoblast reporter line, and analysed the vertebral column at 1mpf. While in controls the osteoblasts were distributed evenly through the arches and centra, *Kita-RAS* showed increased osteoblast signal and patchy distribution, with some regions displaying dense concentrations of osteoblasts while others lacked these cells. Quantification of osteoblasts was performed for two consecutive vertebrae in each fish (n= 3), confirming increase in osteoblasts in *Kita-RAS* (p= 0.0028) (Fig. S5D). Moreover, we detected irregular recruitment of osteoblasts to the chordacentra throughout the vertebral column. Thus, changes in the notochord lead to abnormal osteoblast recruitment and behaviour. Next, we asked whether reduction of inflammatory cells could rescue the bone phenotype. We looked at the vertebral column of controls and *Kita-RAS* + CRISPR (*pu.1* + *gcsfr*) fish at 1mpf by Alizarin Red staining. The severity of the vertebral column phenotype was scored depending on the number of fusions and clefts observed. *Kita-RAS* + CRISPR (*pu.1* + *gcsfr*) partially rescue the vertebral column phenotype (Fig. 6J and K), with a subset of fish showing no fusions or clefts (Fig. 6K). Therefore, modulation of innate immune cells in our chordoma model prevents vertebral fusions and clefts.

Compromised intervertebral discs and impaired bone quality in adult *Kita-RAS*

Embryonic notochordal cells contribute to the formation of the intervertebral disc nucleus pulposus (NP), which plays an important role in regulating disc homeostasis (Choi et al.,

2008). We sought to understand the impact of transformed notochord cells in the adult zebrafish intervertebral disc equivalent regions and vertebral bone. By calculating bone mineral density, we detected a significant TMD decrease in *Kita-RAS* (p= 0.0015) (Fig. 6A and B), indicative of impaired bone quality. We performed histological sections of the adult vertebral column and observed highly fibrotic NP, similar to IVD degeneration (IVDD), with disorganised cellularity found in enlarged vertebrae (Fig. 7A and B). Fibrosis was detected in proximity with the notochord sheath layer. AFOG and Picro-sirius red staining confirmed fibrosis and connectivity with the notochord sheath, showing increased collagen content and increased collagen fibre thickness (Fig. 7B and C). In contrast to IVDD, dehydration did not describe the phenotype of *Kita-RAS* NP, as an increase in glycosaminoglycans was detected (Fig. S5). Additionally, despite fibrosis and disorganisation of the NP, due to cell transformation, we did not observe intervertebral disc calcification, a feature commonly found during IVDD and ageing (Novais et al., 2020b). The outermost component of the discs, the annulus fibrosus (AF), was replaced by bone in IVDs that were compromised by fusions. The structured layers of collagen and elastin that form the zebrafish AF were completely lost in some of the IVDs (Fig. 7D). Interestingly, disorganised and increased number of osteoblasts were detected in the IVD region, corroborating altered osteoblast activity at the endplates of adult fish. The balance between osteoblasts and osteoclasts is key in bone homeostasis and control of bone density. Moreover, osteoclasts are derived from the same cell lineage of macrophages. We performed whole-mount TRAP staining to visualise osteoclast activity. Quantification of TRAP staining revealed exacerbated bone resorption in *Kita-RAS* (p= 0.0026), especially in affected areas of the vertebral column (Fig. S5B and C). Picro-sirius red staining suggested a reduction in collagen fibre thickness in the bone (centra). We quantified the mean intensity of red, green and blue pixels from pictures stained with Picro-sirius red. We detected a significant reduction in red (p= 0.0004) and blue (p= 0.0016)

372 pixels, indicating an abnormal fibre organisation and confirming bone quality impairment in
373 *Kita-RAS* (Fig. 7C). We conclude that transformed cells in the notochord lead to vertebral
374 column and intervertebral disc abnormalities affecting the NP and AF, impairing osteoblasts
375 and osteoclasts activity, consequently altering bone homeostasis in zebrafish.
376

Discussion

"Tumours are wounds that do not heal" was postulated in a classic work published by Harold Dvorak in 1986 (Dvorak, 1986). Dvorak recognized that the composition of the tumour stroma strongly resembled healing skin wounds, suggesting activation of the wound-healing response in the host. Moreover, cancer is frequently the consequence of chronic inflammatory disease (Schafer and Werner, 2008). Given the confined nature of notochordal cells during development of the vertebral column, would pre-neoplastic notochordal cells trigger chronic inflammation as other cancers do? And what is the impact of transformed cells in disc and bone homeostasis? By demonstrating that transformed notochord cells, provoke chronic notochordal wounds and activate wound response mechanisms in zebrafish, leading to inflammation, vertebral column abnormalities and impairment of disc and bone homeostasis, we demonstrated parallels between wound repair, cancer and IVDD in a zebrafish chordoma model.

The *UAS:EGFP-HRASV12* transgene has been successfully used to transform notochordal cells and melanoblasts, contributing to *in vivo* modelling of chordomas and melanomas (Burger et al., 2014, Feng et al., 2010, Santoriello et al., 2010, D'Agati et al., 2019). Here, we made use of the robustness of RAS expression systems to efficiently induce chordomas, using the stable line *Kita-RAS*, an adult melanoma model with notochordal RAS expression. *Kita-RAS* caused similar larval notochord morpho-pathological changes as previously described for *twhh:Gal;UAS:HRASV12* and *4465:Gal;UAS:HRASV12* (Burger et al., 2014), serving as tools to investigate neoplastic notochord cells in adults. While *Kita-RAS* has been extensively used to study melanomas, the vertebral column can still be studied in adult fish without complications of skin tumour, as only around 20% of adult fish develop melanomas (Anelli et al., 2009). Alternatively, *Kita-RAS* when crossed with a pigment free line, such as *casper* (complete lack of melanophores and iridophores) or *nacre* (mutation in

mitfa) (White et al., 2008) can prevent melanoma development. As for *UAS:EGFP-HRASV12* chordoma models, a limitation of the melanoma model is the fact that mutations of RAS members are not common in chordoma. However, RAS-transformed cells lead to activation of downstream signalling driven by EGFR, a cell surface receptor highly involved in chordomas, and mimics upstream receptor tyrosine kinase (RTK) activation (Burger et al., 2014). D'Agati et al, recently demonstrated that while *Brachyury* (*tbxt*) overexpression did not have a tumour-initiating potential to transform notochord cells, when the authors tested RTK, including EGFR, they were able to trigger notochord hyperplasia, suggesting RTK signalling as a possible initiating event in chordoma (D'Agati et al., 2019).

Although human chordomas are thought to originate from hyperplasia of notochordal remnants, benign notochordal remnants are occasionally found and are associated with vertebral abnormalities, such as vertebral clefts and bifurcations (Oner et al., 2006). When we looked at the adult *Kita-RAS* we observed vertebral clefts and hemivertebra that recapitulate human notochordal remnants. However, vertebral malformations might not be a direct effect from pre-neoplastic notochordal cells, but a result from abnormal notochordal cell behaviour. Recent studies have shown that notochord vacuoles function as a hydrostatic scaffold that guides symmetrical growth of vertebrae and spine formation. Vacuole fragmentation caused by mutations in *dstyk* (*spzl* mutant) resulted in vertebral centra malformation and scoliosis (Bagwell et al., 2020, Sun et al., 2020). Similar to our observations, these studies evidenced that abnormal behaviour of notochord vacuolated cells are associated with vertebral malformations like to those of notochordal remnants in human. Furthermore, hemivertebra and clefts were systematically found in another mutant, *spondo*, carrying a mutation in *cmn* (Calimmin, a teleost-specific extracellular matrix protein with weak similarity to Elastin, and expressed in the notochord sheath), due to abnormalities in the notochord sheath layer (Peskin et al., 2020). Here, we demonstrated that destabilisation of the notochord vacuolated

cells also triggered cellular changes in the notochord sheath layer (Fig. 8). Hence, revealing double and overlapping routes in which notochord neoplastic cells compromise the formation of the vertebral column: the inner vacuolated cells and the outer notochord sheath cells.

Notochord damage also leads to vertebral column abnormalities, including fusions and segmentation mispatterning (Lleras Forero et al., 2018, Wopat et al., 2018, Pogoda et al., 2018). We showed that *Kita-RAS* mimicked notochordal damages and induced repair mechanism as demonstrated by activation and invagination of *col9+* notochord sheath cells and expression of *wt1b* in wounded areas, as previously described for notochordal wounds (Lopez-Baez et al., 2018, Garcia et al., 2017). Our findings suggest a key role of the notochord sheath and wound repair in chordoma. Interestingly, when RAS is activated in the notochord sheath specifically with *col2a1a* driving RAS, it also causes chordomas (D'Agati et al., 2019), sustaining a key role of the sheath layer in zebrafish chordomas. As neoplastic cells are continuously modifying the notochord, this causes wounds that seem to progress and remain chronic or unresolved. We showed for the first time that wounding provoked by transformed notochord cells triggers the recruitment of neutrophils and macrophages. Innate immune cells not only were present in higher number but changed their behaviour by prolonging their interaction time with the notochord sheath in wounded regions; in some cases they were able to breach the sealing membrane and achieve direct contact with cancer cells. It has been recently described that inflammatory cells make use of pre-existing holes in the basement membrane to gain access and reach pre-neoplastic cells in a melanoma model (van den Berg et al., 2019). In our chordoma model, inflammatory cells were observed in direct contact with pre-neoplastic cells in regions of severe notochord sheath wounds, which similarly, may serve as breaches in the notochord sheath to allow neutrophils and macrophages to reach pre-neoplastic cells. The interaction between neutrophils/macrophages and transformed cells have been beautifully described for melanoma in zebrafish, with

formation of cytoplasmic tether linking the two cell types and engulfment of transformed cells by neutrophils and macrophages (Feng et al., 2010). H_2O_2, a key damage signal directing recruitment of neutrophils to a wound, was also identified as the major component drawing recruitment of leukocytes to the transformed cells (Feng et al., 2010). Remarkably, when we depleted innate immune cells using morpholinos or CRISPR, we could rescue the notochord phenotype by inhibiting the aberrant proliferation of transformed cells, as demonstrated for melanoma (Feng et al., 2010), and partially rescuing the skeletal phenotype, by showing reduction of vertebral fusions. Thus, highlighting parallels between cancer and wound, and suggesting that immunomodulation might be a promising treatment for chordomas. When zebrafish notochord is infected with *E.coli*, Nguyen-Chi et al showed strong and persistent recruitment of neutrophils and macrophages (Nguyen-Chi et al., 2014). The authors also showed that *il1b* is partially required for recruitment of neutrophils but not macrophages. Fascinatingly, degranulation of neutrophils led to destruction of the host tissues and adult vertebral column defects, involving clefts and fusions. *il1b* morphants reduced neutrophil recruitment and prevented anterior notochord lesions. Altogether, inflammation appears to play an important role in controlling notochord damage and adult bone phenotype (Nguyen-Chi et al., 2014). By showing that mosaic ablation of innate immune cells by CRISPR ameliorate chordoma and the vertebral column phenotype we highlighted potential opportunities for early intervention in the treatment of chordomas and vertebral column fusions.

Kita-RAS fish displayed adult IVDs abnormalities that resembled ageing zebrafish IVDD (unpublished data) with fibrotic NP and disorganised AF. Without parallel in zebrafish, we demonstrated that abnormalities in the early notochord cells and nucleus pulposus prime IVDD. Adult discs showed compromised notochord sheath, visualised by increased thickening of collagen fibres and fibre invasion towards the NP, hence a likely

477 involvement of wound repair mechanisms in adult discs and IVDD. Indeed, human
478 orthologues encoding collagen type IX and collagen type XI are expressed in the notochord
479 sheath and have been associated with IVDD in populational studies (Feng et al., 2016), which
480 supports the involvement of the notochord sheath in IVDD in zebrafish. The inflammatory
481 processes exacerbated by cytokines TNF-α and IL-1β are key events in IVDD (Risbud and
482 Shapiro, 2014), they contribute to IVDD through degradation of extracellular matrix,
483 likewise they are implicated in wounds and cancer. NP fibrosis during degeneration mimics
484 wounds and fibrosis in other tissues (Novais et al., 2020b). *Kita-RAS* also developed bone
485 quality impairment, emphasising nucleus pulposus modifications in regulation of bone
486 homeostasis, suggesting changes in bone metabolic markers during chordomas. We detected
487 increased osteoclast activity and chaotic osteoblasts at the endplates, in addition to osteoblast
488 behaviour abnormalities and abnormal bone homeostasis. Osteoclasts share a common cell
489 lineage with macrophages, and transdifferentiation of macrophages to osteoclasts has been
490 reported (Pereira et al., 2018), suggesting opportunities to treat the bone phenotype through
491 modulation of inflammation. In conclusion, using zebrafish we raised equivalences between
492 chordomas, IVDD and wound repair, highlighting inflammation as a common event for
493 potential therapeutic intervention.
494

Material and Methods

Zebrafish husbandry and lines

Zebrafish were housed as described (Westerfield, 2000). Transgenic lines included: Tg(*kita:Gal4;UAS:mCherry;UAS:HRASG12V-GFP*) (Feng et al. 2010; Santoriello et al. 2010) and Tg(*kita:Gal4;UAS:mCherry;UAS:mCherry-HRASG12V*)(van den Berg et al., 2019) were incrossed to obtain Tg(*kita:Gal4;UAS:HRASG12V-GFP*) and Tg(*kita:Gal4;UAS:mCherry-HRASG12V*), here referred as "*Kita-RAS*", and Tg(*kita:Gal4;UAS:mCherry)* as controls. Tg(*lyz:DsRed*) (Hall et al. 2007); Tg(*mpeg:FRET*) (a gift from Stephen Renshaw at the University of Sheffield); Tg(*col9a2:GFPCaaX*)(Garcia et al., 2017); Tg(*wt1b:GFP*) (Perner et al., 2007); Tg(*entpd5:kaeda*)(Huitema et al., 2012); Tg(*osx:NTR-mCherry*)(Singh et al., 2012). Animal experiments were ethically approved by the University of Bristol Animal Welfare and Ethical Review Body (AWERB) and conducted under UK Home Office project licence.

Cellular proliferation assay

Cellular proliferation was quantified using the Click-iT Plus EdU Alexa Fluor 647 Imaging Kit (Life Technologies, C10640). Larvae were immersed in Danieau's solution containing 100 μM EdU solution and were incubated for 24 h or 48 h at 28.5˚C before termination of the experiment at 5 days post-fertilisation (dpf). Larvae were then fixed in 4% paraformaldehyde (PFA) for 2 h at room temperature with gentle shaking, washed with PBS solution containing 0.5% Triton X-100 (PBST) and 3% (w/v) Bovine Serum Albumin (BSA), and permeabilised in PBST solution containing 1% DMSO for 1 h at room temperature. For EdU detection, larvae were washed in PBST 3% BSA and incubated with the Click-iT Plus reaction cocktail containing Alexa Fluor-647 azide for 30 minutes at room temperature, in accordance with the manufacturers protocol. For quantification, EdU positive cells within and in proximity of the

519 notochord were counted manually through the z stacks from confocal images and similar
520 areas or interest.

521 **Confocal imaging**

522 Live zebrafish were mounted ventrally on coverslips in 1% low-melting point agarose
523 containing MS222 (for live samples) and imaged using a Leica TCS SP8 AOBS confocal
524 laser scanning microscope attached to a Leica DMi8 inverted epifluorescence microscope
525 using 10x dry lens or 20x glycerol lens. The temperature in the chamber covering the
526 microscope was maintained at 28˚C. Movies were recorded at an interval time of 5.45 min or
527 3.75 min per frame and a total time of 60 min or 120 min for neutrophils and macrophages,
528 respectively.

529 **Confocal post-image analysis**

530 Image processing was performed using Fiji (Schneider et al., 2012). 1- Analysis of number
531 and time of neutrophil/macrophage interactions with notochord sheath: neutrophils and
532 macrophages were considered to be interacting with the notochord sheath when they were in
533 direct surface contact with the sheath layer. The number of these interactions and their
534 duration were manually quantified from time-lapse movies in a pre-defined region of the
535 flank above the caudal hematopoietic tissue in the zebrafish larva, from the total field of
536 view. Neutrophils, macrophages and notochord were identified by visualisation of their
537 fluorescence in the fluorescent channel while the notochord sheath was more accurately
538 distinguished by visualisation in the brightfield channel. Movies were exported from Fiji as
539 QuickTime movies to play at 3 frames per sec. 2- Analysis of osteoblasts: images were
540 converted to 32-bit, applied LUT (16 colours), flattened and then saved as tiff images. The
541 tiff files were imported to Fiji, two consecutive vertebrae were selected using the freehand
542 selection tool, from which the mean pixel intensity values were calculated. 3- Analysis of the

area of notochord sheath cells (*col9a2+*): *Kita-RAS* notochord was divided in wound-proximal and wound-distal regions. Using the freehand selection tool in Fiji, the area of 10 cells were analysed per region, using 10 fish for controls and *Kita-RAS*.

Morpholino (MO) injections

Previously described morpholinos including *pu.1* MO (5′-GATATACTGATACTCCATTGGTGGT-3′) (0.2 mM) (Rhodes et al., 2005), *gcsfr* MO (5′-GAAGCACAAGCGAGACGGATGCCAT-3′) (0.3 mM) (Liongue et al., 2009) and a scrambled MO (5'- CCTCTTACCTCAGTTACAATTTATA- 3') (0.5 mM) (GeneTools LLC, USA) were injected into 1-cell stage embryos, as previously described (Liongue et al., 2009, Rhodes et al., 2005, van den Berg et al., 2019).

CRISPR/Cas9 injections

We used three synthetic gRNAs targeting each of the genes, *pu.1(spi1b)* and *csf3r(gcsfr)*, ordered as crRNAs (Sigma). We used the same target sites for *gcsfr* as previously described (Yang et al., 2020), while for *pu.1we* targeted the same genomic region as previously described in a pu.1 mutant (chr7:32655153-32655197) (Yang et al., 2020). Pu.1 target sequences: pu.1 cr1 GAGGGATGTGATGGCTACCC, pu.1 cr2 AGCTCTGTAAAGTGGCTCTC and pu.1 cr3 GCCTGGGTCCATGAAATGGC). All six crRNAs (2pg) were incubated with tracrRNA (10pg) and GeneArt Platinum Cas9 nuclease (Invitrogen) prior to injections. Injections were performed into 1-cell stage embryos as previously described (Brunt et al., 2017). To validate CRISPR efficiency, DNA was extracted from 12 individual injected larvae at 5dpf, followed by PCR amplification with FAM-M13F primer and gene-specific primers, with each forward primer containing an M13 tail (pu.1 F: TGTAAAACGACGGCCAGTCCGTGTCTAGATCACTCTTGGG; pu.1 R: AAACCAAACCATAAATGATTCGTTTT; csf3r F: TGTAAAACGACGGCCAGTGATTGCTGACGTAACTATTGTAC; csf3r R:

CTCACATTTAAAGTCTTATCAG). PCRs were submitted to fragment length analysis (ABI 3500)(Carrington et al., 2015). Controls were injected with Cas9 protein and SygRNA® SpCas9 tracrRNA (10pg) (Merck). Images of the notochord were acquired at 5dpf using a Leica fluorescent stereomicroscopy (MZ10F), followed by analysis of notochord lesions.

Analysis of notochord lesions

Notochord images of 5dpf larvae previously injected with MO or CRISPR were analysed using custom Python scripts and by implementing three steps. First, we detected pixels of the notochord through manually setting the value of the intensity threshold. Second, we fit the pixels with a 6th order polynomial function to obtain the intensity profile along the notochord. Specifically, the intensity profile was measured along the polynomial fit inside the image, using the algorithm adapted from the scikit-image package (van der Walt et al., 2014), where we modified the function “profile line” to work with a polynomial line. The average value of the intensity profile was used as a measurement of the severity of lesions within the notochord. Finally, the average intensity from the notochord was compared among different groups. For statistical analysis we used ANOVA and Kruskal-Wallis H-test, implemented in scipy (Virtanen et al., 2020). Dunn’s method was used for multiple comparison test, implemented in scikit-posthocs (Terpilowski, 2019), p values were adjusted with Bonferroni.

Alizarin Red and Calcein staining

Alizarin Red S staining was performed in fixed fish to label calcified tissues and carried out using standard protocols (Walker and Kimmel, 2007). Live Calcein or Alizarin Red S staining was carried out as previously described (Bensimon-Brito et al., 2016). 14dpf fish were fixed in 4%PFA and undergone Alizarin Red staining. Pictures of the entire fish were taken under a Leica stereomicroscope. Total fish length and the length of the first seven vertebral segments were measured using Leica LAS X Software.

Vertebral column severity scoring system

Alizarin Red S staining was performed in fixed samples of 1 month old fish (1mpf) (*Kita* control n= 47 ; *Kita-RAS* n = 61; and *Kita-RAS +CRISPR* n= 97), and pictures taken with a Leica stereomicroscope (MZ10F). The length of each fish was measured from the nose to the most posterior extremity of the vertebral column, the tail fin was not included in the measurement. Those fish in which the vertebral columns were not completely formed were excluded from our severity score analysis. The vertebral column severity scoring system was based on numbers of fusions and clefts identified in each fish. Fusions and clefts were scored independently. Score of 3: $n \geq 5$; score of 2: $3<n<5$; score of 1: $n \leq 3$; score of 0: n=0 (n= number of fusions and clefts).

Radiographs (X-ray)

Live 1 year old fish (1y) were anaesthetised with MS222 and radiographed using a MultiFocus digital radiography system (Faxitron) under 2x zoom and using the settings: 45 kv, 5 seconds of exposure and 0.46. A total of 118 fish were X-rayed (controls, n = 40; *Kita-RAS*, n = 78). Fish lengths were measured using Fiji (Schindelin et al., 2012) (in pixels), using images that were acquired under the same conditions.

Micro-computed tomography (µCT)

Six month old fish (6mpf) were fixed in 4% PFA for 14 days, followed by sequential washes in ethanol and maintained in a 70% ethanol solution. Micro-computed tomography (µCT) was performed using a Nikon X-TEK 225 HT CT scanner under an X-ray source of 130 kV, 53 µA without additional filters. Whole fish were scanned at voxel size of 20 µm, and selected spine regions rescanned at 5 µm. Images were reconstructed using CT Pro 3D software (Nikon). Amira 6.0 (FEI) was used to generate 3D volume and surface renders for image acquisition. For calculations of tissue mineral density (TMD), defined as measurement

616 restricted to within the volume of calcified bone tissue (Bouxsein et al., 2010), the centrae
617 were segmented and the mean grey values retrieved. Grey values were calibrated with
618 phantoms of known densities (0.25 and 0.75 $g.cm^3$ of CaHA), and used for density
619 calculations, as previously described (Kague et al., 2019). Three fish from each group were
620 used for TMD calculation.

621 **Histology**

622 Adult fish (3mpf, control, n = 3; *Kita-RAS*, n = 3) were fixed in 4% PFA for 14 days, then
623 decalcified in 1M EDTA solution for 20 days at room temperature. Larvae (control, n = 3;
624 *Kita-RAS*, n = 4) were fixed for 2 hours. Samples were dehydrated in ethanol, embedded in
625 paraffin and sagittal sections were taken at 8 µm thickness. Selected slides were de-waxed
626 and stained with Toluidine Blue (Kague et al., 2018)**,** Alcian Blue, AFOG or Picro-sirius red,
627 as performed elsewhere (Hayes et al., 2013). Images were acquired on a Leica DMI600
628 inverted microscope, using 20X and 40X oil objectives, LAS software and a DFC420C
629 colour camera. Quantification of thickness of collagen fibre was performed using Fiji
630 (Schindelin et al., 2012), by selecting an area of interest within the bone, followed by
631 measurement of mean intensity of red, blue and green pixels.

632 **Tartrate-resistant acid phosphatase (TRAP) staining**

633 TRAP staining was performed in whole-mount 3 month old fish (3mpf) (control, n = 4; *Kita-*
634 *RAS*, n = 5) using Acid Phosphatase, Leukocyte (TRAP) kit (Merck, cat 387A) and
635 following the instructions provided by the manufacture. Fish were fixed overnight in fixative
636 solution (provided). Samples were washed for 15 min in distilled water, followed by
637 permeabilization using 1% trypsin in 30% borate solution at 37˚C overnight. Fish were
638 incubated in TRAP staining solution (provided) at 37˚C for 6h in the dark, followed by two
639 washes of 10 min each in distilled water. Pigmentation was removed by incubating the
640 specimens in 3% H_2O_2. Pictures were taken from dissected spines placed in 70% glycerol

under a Leica stereomicroscope. Quantification of TRAP signal was performed using Fiji (Schindelin et al., 2012). Images were converted to 32-bit, and LUT (physics) applied. We inverted the LUT, flattened the images and calculated the mean of red pixels, correspondent to high TRAP signal.

Statistical Analysis

GraphPad Prism 8 was used for statistical analyses. The statistical test used for each panel can be found in the correspondent figure legend. Statistical significance is indicated on graphs with the p value.

Acknowledgements

Thank you to Prof Stefan Schulte-Merker and his lab for sharing the lines: Tg(*col9a2:GFPCaaX*) and Tg(*wt1b:GFP*) used in this work. We thank all members of the Wolfson Bioimaging Facility at the University of Bristol for support and assistance in this work. We are grateful to all members of the Histology Service Unit and the Zebrafish Facility of the University of Bristol for their services and contribution. Faxitron for kindly lending us the X-ray machine. Finally, we thank Prof Paul Martin for proofreading the manuscript and his support.

Conflicts of interest

We declare no competing interests.

Funding

EK and CH were funded by Versus Arthritis (21937, 21211). PL was funded by the Spanish Rafael del Pino Foundation. YY was funded by the China Scholarship Council. This work was supported by grant MR/N0137941/1 for the GW4 BIOMED DTP, awarded to the Universities of Bath, Bristol, Cardiff and Exeter from the Medical Research Council (MRC)/UKRI.

Data availability

Data will be available via a DOI at data.bris. Code will be provided upon request.

Author contributions

PL, LD, and EK performed experiments. PL, LD, YY and EK analysed data. The project was designed by EK. YY developed computational analysis for quantification of notochord lesions. All authors contributed to drafting and reviewing the manuscript.

References

ANELLI, V., SANTORIELLO, C., DISTEL, M., KOSTER, R. W., CICCARELLI, F. D. & MIONE, M. 2009. Global repression of cancer gene expression in a zebrafish model of melanoma is linked to epigenetic regulation. *Zebrafish,* 6**,** 417-24.

BAGWELL, J., NORMAN, J., ELLIS, K., PESKIN, B., HWANG, J., GE, X., NGUYEN, S. V., MCMENAMIN, S. K., STAINIER, D. Y. & BAGNAT, M. 2020. Notochord vacuoles absorb compressive bone growth during zebrafish spine formation. *Elife,* 9.

BARRY, J. J., JIAN, B. J., SUGHRUE, M. E., KANE, A. J., MILLS, S. A., TIHAN, T. & PARSA, A. T. 2011. The next step: innovative molecular targeted therapies for treatment of intracranial chordoma patients. *Neurosurgery,* 68**,** 231-40; discussion 240-1.

BENSIMON-BRITO, A., CARDEIRA, J., DIONISIO, G., HUYSSEUNE, A., CANCELA, M. L. & WITTEN, P. E. 2016. Revisiting in vivo staining with alizarin red S--a valuable approach to analyse zebrafish skeletal mineralization during development and regeneration. *BMC Dev Biol,* 16**,** 2.

BERGEN, D. J. M., KAGUE, E. & HAMMOND, C. L. 2019. Zebrafish as an Emerging Model for Osteoporosis: A Primary Testing Platform for Screening New Osteo-Active Compounds. *Front Endocrinol (Lausanne),* 10**,** 6.

BOUXSEIN, M. L., BOYD, S. K., CHRISTIANSEN, B. A., GULDBERG, R. E., JEPSEN, K. J. & MULLER, R. 2010. Guidelines for assessment of bone microstructure in rodents using micro-computed tomography. *J Bone Miner Res,* 25**,** 1468-86.

BRUNT, L. H., BEGG, K., KAGUE, E., CROSS, S. & HAMMOND, C. L. 2017. Wnt signalling controls the response to mechanical loading during zebrafish joint development. *Development,* 144**,** 2798-2809.

BURGER, A., VASILYEV, A., TOMAR, R., SELIG, M. K., NIELSEN, G. P., PETERSON, R. T., DRUMMOND, I. A. & HABER, D. A. 2014. A zebrafish model of chordoma initiated by notochord-driven expression of HRASV12. *Dis Model Mech,* 7**,** 907-13.

CARRINGTON, B., VARSHNEY, G. K., BURGESS, S. M. & SOOD, R. 2015. CRISPR-STAT: an easy and reliable PCR-based method to evaluate target-specific sgRNA activity. *Nucleic Acids Res,* 43**,** e157.

CHIA, K., MAZZOLINI, J., MIONE, M. & SIEGER, D. 2018. Tumor initiating cells induce Cxcr4-mediated infiltration of pro-tumoral macrophages into the brain. *Elife,* 7.

CHOI, K. S., COHN, M. J. & HARFE, B. D. 2008. Identification of nucleus pulposus precursor cells and notochordal remnants in the mouse: implications for disk degeneration and chordoma formation. *Dev Dyn,* 237**,** 3953-8.

CHUGH, R., TAWBI, H., LUCAS, D. R., BIERMANN, J. S., SCHUETZE, S. M. & BAKER, L. H. 2007. Chordoma: the nonsarcoma primary bone tumor. *Oncologist,* 12**,** 1344-50.

D'AGATI, G., CABELLO, E. M., FRONTZEK, K., RUSHING, E. J., KLEMM, R., ROBINSON, M. D., WHITE, R. M., MOSIMANN, C. & BURGER, A. 2019. Active receptor tyrosine kinases, but not Brachyury, are sufficient to trigger chordoma in zebrafish. *Dis Model Mech,* 12.

DALLAS, S. L. & BONEWALD, L. F. 2010. Dynamics of the transition from osteoblast to osteocyte. *Ann N Y Acad Sci,* 1192**,** 437-43.

DE BRUINE, F. T. & KROON, H. M. 1988. Spinal chordoma: radiologic features in 14 cases. *AJR Am J Roentgenol,* 150**,** 861-3.

DISTEL, M., WULLIMANN, M. F. & KOSTER, R. W. 2009. Optimized Gal4 genetics for permanent gene expression mapping in zebrafish. *Proc Natl Acad Sci U S A,* 106**,** 13365-70.

DVORAK, H. F. 1986. Tumors: wounds that do not heal. Similarities between tumor stroma generation and wound healing. *N Engl J Med,* 315**,** 1650-9.

EMING, S. A., WYNN, T. A. & MARTIN, P. 2017. Inflammation and metabolism in tissue repair and regeneration. *Science,* 356**,** 1026-1030.

FENG, Y., EGAN, B. & WANG, J. 2016. Genetic Factors in Intervertebral Disc Degeneration. *Genes Dis,* 3**,** 178-185.

FENG, Y., RENSHAW, S. & MARTIN, P. 2012. Live imaging of tumor initiation in zebrafish larvae reveals a trophic role for leukocyte-derived PGE(2). *Curr Biol,* 22**,** 1253-9.

FENG, Y., SANTORIELLO, C., MIONE, M., HURLSTONE, A. & MARTIN, P. 2010. Live imaging of innate immune cell sensing of transformed cells in zebrafish larvae: parallels between tumor initiation and wound inflammation. *PLoS Biol,* 8**,** e1000562.

FLEMING, A., KEYNES, R. & TANNAHILL, D. 2004. A central role for the notochord in vertebral patterning. *Development,* 131**,** 873-80.

FREISINGER, C. M. & HUTTENLOCHER, A. 2014. Live imaging and gene expression analysis in zebrafish identifies a link between neutrophils and epithelial to mesenchymal transition. *PLoS One,* 9**,** e112183.

GARCIA, J., BAGWELL, J., NJAINE, B., NORMAN, J., LEVIC, D. S., WOPAT, S., MILLER, S. E., LIU, X., LOCASALE, J. W., STAINIER, D. Y. R. & BAGNAT, M. 2017. Sheath Cell Invasion and Trans-differentiation Repair Mechanical Damage Caused by Loss of Caveolae in the Zebrafish Notochord. *Curr Biol,* 27**,** 1982-1989 e3.

GBD, INJURY, I. & PREVALENCE, C. 2017. Global, regional, and national incidence, prevalence, and years lived with disability for 328 diseases and injuries for 195 countries, 1990-2016: a systematic analysis for the Global Burden of Disease Study 2016. *Lancet,* 390**,** 1211-1259.

HAYES, A. J., REYNOLDS, S., NOWELL, M. A., MEAKIN, L. B., HABICHER, J., LEDIN, J., BASHFORD, A., CATERSON, B. & HAMMOND, C. L. 2013. Spinal deformity in aged zebrafish is accompanied by degenerative changes to their vertebrae that resemble osteoarthritis. *PLoS One,* 8**,** e75787.

HUITEMA, L. F., APSCHNER, A., LOGISTER, I., SPOORENDONK, K. M., BUSSMANN, J., HAMMOND, C. L. & SCHULTE-MERKER, S. 2012. Entpd5 is essential for skeletal mineralization and regulates phosphate homeostasis in zebrafish. *Proc Natl Acad Sci U S A,* 109**,** 21372-7.

KAGUE, E., HUGHES, S. M., LAWRENCE, E. A., CROSS, S., MARTIN-SILVERSTONE, E., HAMMOND, C. L. & HINITS, Y. 2019. Scleraxis genes are required for normal musculoskeletal development and for rib growth and mineralization in zebrafish. *FASEB J,* 33**,** 9116-9130.

KAGUE, E., WITTEN, P. E., SOENENS, M., CAMPOS, C. L., LUBIANA, T., FISHER, S., HAMMOND, C., BROWN, K. R., PASSOS-BUENO, M. R. & HUYSSEUNE, A. 2018. Zebrafish sp7 mutants show tooth cycling independent of attachment, eruption and poor differentiation of teeth. *Dev Biol,* 435**,** 176-184.

KATSUURA, Y. & KIM, H. J. 2019. Butterfly Vertebrae: A Systematic Review of the Literature and Analysis. *Global Spine J,* 9**,** 666-679.

LIONGUE, C., HALL, C. J., O'CONNELL, B. A., CROSIER, P. & WARD, A. C. 2009. Zebrafish granulocyte colony-stimulating factor receptor signaling promotes myelopoiesis and myeloid cell migration. *Blood,* 113**,** 2535-46.

LLERAS FORERO, L., NARAYANAN, R., HUITEMA, L. F., VANBERGEN, M., APSCHNER, A., PETERSON-MADURO, J., LOGISTER, I., VALENTIN, G., MORELLI, L. G., OATES, A. C. & SCHULTE-MERKER, S. 2018. Segmentation of the zebrafish axial skeleton relies on notochord sheath cells and not on the segmentation clock. *Elife,* 7.

LOPEZ-BAEZ, J. C., SIMPSON, D. J., L, L. L. F., ZENG, Z., BRUNSDON, H., SALZANO, A., BROMBIN, A., WYATT, C., RYBSKI, W., HUITEMA, L. F. A., DALE, R. M., KAWAKAMI, K., ENGLERT, C., CHANDRA, T., SCHULTE-MERKER, S., HASTIE, N. D. & PATTON, E. E. 2018. Wilms Tumor 1b defines a wound-specific sheath cell subpopulation associated with notochord repair. *Elife,* 7.

MACCARTHY-MORROGH, L. & MARTIN, P. 2020. The hallmarks of cancer are also the hallmarks of wound healing. *Sci Signal,* 13.

MCMASTER, M. L., GOLDSTEIN, A. M. & PARRY, D. M. 2011. Clinical features distinguish childhood chordoma associated with tuberous sclerosis complex (TSC) from chordoma in the general paediatric population. *J Med Genet,* 48**,** 444-9.

NGUYEN-CHI, M., PHAN, Q. T., GONZALEZ, C., DUBREMETZ, J. F., LEVRAUD, J. P. & LUTFALLA, G. 2014. Transient infection of the zebrafish notochord with E. coli induces chronic inflammation. *Dis Model Mech,* 7**,** 871-82.

NOVAIS, E. J., TRAN, V. A., MIAO, J., SLAVER, K., SINENSKY, A., DYMENT, N. A., ADDYA, S., SZERI, F., VAN DE WETERING, K., SHAPIRO, I. M. & RISBUD, M. V. 2020a. Comparison of inbred mouse strains shows diverse phenotypic outcomes of intervertebral disc aging. *Aging Cell*.

NOVAIS, E. J., TRAN, V. A., MIAO, J., SLAVER, K., SINENSKY, A., DYMENT, N. A., ADDYA, S., SZERI, F., VAN DE WETERING, K., SHAPIRO, I. M. & RISBUD, M. V. 2020b. Comparison of inbred mouse strains shows diverse phenotypic outcomes of intervertebral disc aging. *Aging Cell,* 19**,** e13148.

ONER, A. Y., AKPEK, S. & TOKGOZ, N. 2006. Persistent notochordal canal mimicking compression fracture: a case report. *Acta Radiol,* 47**,** 875-7.

PEREIRA, M., PETRETTO, E., GORDON, S., BASSETT, J. H. D., WILLIAMS, G. R. & BEHMOARAS, J. 2018. Common signalling pathways in macrophage and osteoclast multinucleation. *J Cell Sci,* 131.

PERNER, B., ENGLERT, C. & BOLLIG, F. 2007. The Wilms tumor genes wt1a and wt1b control different steps during formation of the zebrafish pronephros. *Dev Biol,* 309**,** 87-96.

PESKIN, B., HENKE, K., CUMPLIDO, N., TREASTER, S., HARRIS, M. P., BAGNAT, M. & ARRATIA, G. 2020. Notochordal Signals Establish Phylogenetic Identity of the Teleost Spine. *Curr Biol*.

POGODA, H. M., RIEDL-QUINKERTZ, I., LOHR, H., WAXMAN, J. S., DALE, R. M., TOPCZEWSKI, J., SCHULTE-MERKER, S. & HAMMERSCHMIDT, M. 2018. Direct activation of chordoblasts by retinoic acid is required for segmented centra mineralization during zebrafish spine development. *Development,* 145.

RENSHAW, S. A. & TREDE, N. S. 2012. A model 450 million years in the making: zebrafish and vertebrate immunity. *Dis Model Mech,* 5**,** 38-47.

RHODES, J., HAGEN, A., HSU, K., DENG, M., LIU, T. X., LOOK, A. T. & KANKI, J. P. 2005. Interplay of pu.1 and gata1 determines myelo-erythroid progenitor cell fate in zebrafish. *Dev Cell,* 8**,** 97-108.

RISBUD, M. V. & SHAPIRO, I. M. 2014. Role of cytokines in intervertebral disc degeneration: pain and disc content. *Nat Rev Rheumatol,* 10**,** 44-56.

RODRIGUES-PINTO, R., RICHARDSON, S. M. & HOYLAND, J. A. 2014. An understanding of intervertebral disc development, maturation and cell phenotype provides clues to direct cell-based tissue regeneration therapies for disc degeneration. *Eur Spine J,* 23**,** 1803-14.

ROH-JOHNSON, M., SHAH, A. N., STONICK, J. A., POUDEL, K. R., KARGL, J., YANG, G. H., DI MARTINO, J., HERNANDEZ, R. E., GAST, C. E., ZAROUR, L. R., ANTOKU, S., HOUGHTON, A. M., BRAVO-CORDERO, J. J., WONG, M. H., CONDEELIS, J. & MOENS, C. B. 2017. Macrophage-Dependent Cytoplasmic Transfer during Melanoma Invasion In Vivo. *Dev Cell,* 43**,** 549-562 e6.

SALISBURY, J. R. 1993. The pathology of the human notochord. *J Pathol,* 171**,** 253-5.

SANTORIELLO, C., GENNARO, E., ANELLI, V., DISTEL, M., KELLY, A., KOSTER, R. W., HURLSTONE, A. & MIONE, M. 2010. Kita driven expression of oncogenic HRAS leads to early onset and highly penetrant melanoma in zebrafish. *PLoS One,* 5**,** e15170.

SCHAFER, M. & WERNER, S. 2008. Cancer as an overhealing wound: an old hypothesis revisited. *Nat Rev Mol Cell Biol,* 9**,** 628-38.

SCHINDELIN, J., ARGANDA-CARRERAS, I., FRISE, E., KAYNIG, V., LONGAIR, M., PIETZSCH, T., PREIBISCH, S., RUEDEN, C., SAALFELD, S., SCHMID, B., TINEVEZ, J. Y., WHITE, D. J., HARTENSTEIN, V., ELICEIRI, K., TOMANCAK, P. & CARDONA, A. 2012. Fiji: an open-source platform for biological-image analysis. *Nat Methods,* 9**,** 676-82.

SCHNEIDER, C. A., RASBAND, W. S. & ELICEIRI, K. W. 2012. NIH Image to ImageJ: 25 years of image analysis. *Nat Methods,* 9**,** 671-5.

SINGH, S. P., HOLDWAY, J. E. & POSS, K. D. 2012. Regeneration of amputated zebrafish fin rays from de novo osteoblasts. *Dev Cell,* 22**,** 879-86.

STACCHIOTTI, S., GRONCHI, A., FOSSATI, P., AKIYAMA, T., ALAPETITE, C., BAUMANN, M., BLAY, J. Y., BOLLE, S., BORIANI, S., BRUZZI, P., CAPANNA, R., CARACENI, A., CASADEI, R., COLIA, V., DEBUS, J., DELANEY, T., DESAI, A., DILEO, P., DIJKSTRA, S., DOGLIETTO, F., FLANAGAN, A., FROELICH, S., GARDNER, P. A., GELDERBLOM, H., GOKASLAN, Z. L., HAAS, R., HEERY, C., HINDI, N., HOHENBERGER, P., HORNICEK, F., IMAI, R., JEYS, L., JONES, R. L., KASPER, B., KAWAI, A., KRENGLI, M., LEITHNER, A., LOGOWSKA, I., MARTIN BROTO, J., MAZZATENTA, D., MOROSI, C., NICOLAI, P., NORUM, O. J., PATEL, S., PENEL, N., PICCI, P., PILOTTI, S., RADAELLI, S., RICCHINI, F., RUTKOWSKI, P., SCHEIPL, S., SEN, C., TAMBORINI, E., THORNTON, K. A., TIMMERMANN, B., TORRI, V., TUNN, P. U., UHL, M., YAMADA, Y., WEBER, D. C., VANEL, D., VARGA, P. P., VLEGGEERT-LANKAMP, C. L. A., CASALI, P. G. & SOMMER, J. 2017. Best practices for the management of local-regional recurrent chordoma: a position paper by the Chordoma Global Consensus Group. *Ann Oncol,* 28**,** 1230-1242.

STEMPLE, D. L. 2005. Structure and function of the notochord: an essential organ for chordate development. *Development,* 132**,** 2503-12.

SUN, X., ZHOU, Y., ZHANG, R., WANG, Z., XU, M., ZHANG, D., HUANG, J., LUO, F., LI, F., NI, Z., ZHOU, S., CHEN, H., CHEN, S., CHEN, L., DU, X., CHEN, B., HUANG, H., LIU, P., YIN, L., QIU, J., CHEN, D., DENG, C., XIE, Y., LUO, L. & CHEN, L. 2020. Dstyk mutation leads to congenital scoliosis-like vertebral malformations in zebrafish via dysregulated mTORC1/TFEB pathway. *Nat Commun,* 11**,** 479.

TERPILOWSKI 2019. scikit-posthocs: Pairwise multiple comparison tests in Python. *Journal of Open Source Software,* 4(36)**,** 1169.

VAN DEN BERG, M. C. W., MACCARTHY-MORROGH, L., CARTER, D., MORRIS, J., RIBEIRO BRAVO, I., FENG, Y. & MARTIN, P. 2019. Proteolytic and Opportunistic Breaching of the Basement Membrane Zone by Immune Cells during Tumor Initiation. *Cell Rep,* 27**,** 2837-2846 e4.

VAN DER WALT, S., SCHONBERGER, J. L., NUNEZ-IGLESIAS, J., BOULOGNE, F., WARNER, J. D., YAGER, N., GOUILLART, E., YU, T. & SCIKIT-IMAGE, C. 2014. scikit-image: image processing in Python. *PeerJ,* 2**,** e453.

VIRTANEN, P., GOMMERS, R., OLIPHANT, T. E., HABERLAND, M., REDDY, T., COURNAPEAU, D., BUROVSKI, E., PETERSON, P., WECKESSER, W., BRIGHT, J., VAN DER WALT, S. J., BRETT, M., WILSON, J., MILLMAN, K. J., MAYOROV, N., NELSON, A. R. J., JONES, E., KERN, R., LARSON, E., CAREY, C. J., POLAT, I., FENG, Y., MOORE, E. W., VANDERPLAS, J., LAXALDE, D., PERKTOLD, J., CIMRMAN, R., HENRIKSEN, I., QUINTERO, E. A., HARRIS, C. R., ARCHIBALD, A. M., RIBEIRO, A. H., PEDREGOSA, F., VAN MULBREGT, P. & SCIPY, C. 2020. SciPy 1.0: fundamental algorithms for scientific computing in Python. *Nat Methods,* 17**,** 261-272.

VUJOVIC, S., HENDERSON, S., PRESNEAU, N., ODELL, E., JACQUES, T. S., TIRABOSCO, R., BOSHOFF, C. & FLANAGAN, A. M. 2006. Brachyury, a crucial regulator of notochordal development, is a novel biomarker for chordomas. *J Pathol,* 209**,** 157-65.

WALKER, M. B. & KIMMEL, C. B. 2007. A two-color acid-free cartilage and bone stain for zebrafish larvae. *Biotech Histochem,* 82**,** 23-8.

WANG, F., GAO, Z. X., CAI, F., SINKEMANI, A., XIE, Z. Y., SHI, R., WEI, J. N. & WU, X. T. 2017. Formation, function, and exhaustion of notochordal cytoplasmic vacuoles within intervertebral disc: current understanding and speculation. *Oncotarget,* 8**,** 57800-57812.

WESTERFIELD, M. 2000. *The zebrafish book. A guide for the laboratory use of zebrafish (Danio rerio).* Univ. of Oregon Press, Eugene

WHITE, R. M., SESSA, A., BURKE, C., BOWMAN, T., LEBLANC, J., CEOL, C., BOURQUE, C., DOVEY, M., GOESSLING, W., BURNS, C. E. & ZON, L. I. 2008. Transparent adult zebrafish as a tool for in vivo transplantation analysis. *Cell Stem Cell,* 2**,** 183-9.

WOPAT, S., BAGWELL, J., SUMIGRAY, K. D., DICKSON, A. L., HUITEMA, L. F. A., POSS, K. D., SCHULTE-MERKER, S. & BAGNAT, M. 2018. Spine Patterning Is Guided by Segmentation of the Notochord Sheath. *Cell Rep,* 22**,** 2026-2038.

873 YAMAGUCHI, T., SUZUKI, S., ISHIIWA, H. & UEDA, Y. 2004. Intraosseous benign notochordal cell
874 tumours: overlooked precursors of classic chordomas? *Histopathology,* 44**,** 597-602.
875 YANG, L., JIMENEZ, J. A., EARLEY, A. M., HAMLIN, V., KWON, V., DIXON, C. T. & SHIAU, C. E. 2020.
876 Drainage of inflammatory macromolecules from the brain to periphery targets the liver for
877 macrophage infiltration. *Elife,* 9.
878 ZHENG, C. J. & CHEN, J. 2015. Disc degeneration implies low back pain. *Theor Biol Med Model,* 12**,**
879 24.

880

881

Figure Legends

Figure 1. *Kita* drives RAS expression in the notochord inducing fibrosis and wound-like phenotype. A) Schematic of the wild-type notochord. The notochord is a rod tube formed by a sealing notochord sheath epithelium (nse) layer that wraps the notochord vacuolated cells (nvc). B) Maximum projection from confocal images of control (*Kita:mCherry*) and *Kita-RAS-mCherry* (*Kita-RAS*) at 5dpf. *Kita* drives expression of the reporter and RAS in the notochord cells (magenta arrows), leading to dramatic changes in the notochord. Gaps between vacuolated notochord cells (blue arrows) are filled with small non-vacuolated cells. C) Histological sections of 5dpf control (*Kita-mCherry*) and *Kita-RAS* larvae, stained with Toluidine Blue (T Blue) and AFOG. Control fish show an intact nse. *Kita-RAS* show disruptions of the nse (arrowheads), accumulation of non-vacuolated cells within the notochord (arrow) and fibrous tissue (AFOG, dashed arrow). D) Cross-section from confocal images of *Kita* (control) and *Kita-RAS* at 5dpf, treated for EdU from 2-4dpf to show cell proliferation. Note increased proliferation in the notochord sheath (arrowhead) and within wounded areas of the notochord (arrow). E) Quantification of cell proliferation was performed by counting the number of EdU-positive (+) cells in the control (*Kita*) (n= 8) and *Kita-RAS* (n= 9). Nonparametric t-Test, post hoc Mann-Witney test; data are mean SD. P values are indicated. All scale bars = 50 µm.

Figure 2. Transformed notochord cells alter the organisation of the sheath layer and activate wound repair mechanisms. A) Schematic of the notochord and notochord sheath epithelium (nse) at 5dpf, formed by cells that highly express collagen type IX. B) Confocal images showing maximum projection (Max proj), and cross sections (C section) of *col9a2:GFPCaaX* (nse) and *Kita-mCherry* (notochord cells) in control and *Kita-RAS*, at 5dpf. In *Kita-RAS*, a "scar" region within the notochord (arrowhead) express *col9a2*, and shows connectivity with the nse (arrow). C) The area (white dashed line) of notochord sheath cells

were analysed in controls and within two regions of *Kita-RAS* expressing *col9a2:GFPCaaX:* proximal (wp, magenta dashed line) and distal (wd, magenta solid line) to the wound (arrowhead). D) Graph showing cell area quantification of each group (10 cells were measured for each group and region, and n=10 fish per group). Nested One-Way ANOVA and Tukey's multiple comparisons test were used for statistical analysis. Graph shows mean with SD, p are indicated when significant ($p<0.05$). E) Maximum projection from confocal images showing expression of *wt1b:gfp* in the wounded regions (arrowheads) of *Kita-RAS*. *w1b* is not expressed in controls. All scale bars = 50 µm.

Figure 3. Increased inflammatory response detected in the notochord sheath of *Kita-RAS*. A) Maximum projection from confocal images of the notochord at 5dpf in control (*Kita-mCherry*) and *Kita-RAS* showing neutrophils (cyan arrowhead) interacting by contact with the notochord sheath layer. B) Number of neutrophils interacting with the notochord sheath during the time-lapse (controls n= 6 fish, *Kita-RAS* n= 14 fish). C) Interaction time between neutrophils and the notochord sheath during the time-lapse movies. Each dot represents one neutrophil (controls n=8 neutrophils, n = 4 fish; *Kita-RAS* n =39 neutrophils, n= 14 fish). D) Maximum projection from confocal images of the notochord of 5dpf control (*Kita-mCherry*) and *Kita-RAS* fish showing macrophages (cyan arrowhead) interacting by contact with the notochord sheath. E) Number of macrophages interacting with the notochord sheath during the time-lapse (controls n= 14 fish, *Kita-RAS* n= 15 fish). F) Interaction time between macrophages and the notochord sheath during the time-lapse movies. Each dot represents one macrophage (controls n= 51 macrophages, n= 13 fish; *Kita-RAS* n= 95 macrophages and n= 15 fish). Unpaired, nonparametric t-test, and Mann-Whitney test were used for all graphs. Graphs show mean with SD, p values are indicated when significant ($p<0.05$). All scale bars = 50 µm.

Figure 4. Modulation of the innate immune response prevents chordoma

A) Schematics of the experiment. *Kita-RAS-GFP* were incrossed, embryos from the same cross were divided in three groups: controls, morpholinos (MO) or CRISPR targeting *pu.1* + *gcsfr* (for depletion of neutrophils and macrophages). Injections were carried out at 1-cel stage. The notochords were subsequently imaged and analysed at 5dpf. B) Graph displaying % of neutrophils per area in *Kita-RAS* (control group n= 26) and *Kita-RAS* injected with either morpholinos (MO) (n = 9) or CRISPRs (n= 15). C) Graph showing numbers of macrophages in *Kita-RAS* (n= 14) and *Kita-RAS* injected with either morpholinos (MO) (n = 15) or CRISPRs (n= 19). D) For quantification of neutrophils and macrophages, injections were carried out in Tg(*Lyz:DsRed;mpeg:FRET:Kita:mCherry*). Percentage of neutrophils was calculated within the selected area (red dashed region), after image binarization. Numbers of macrophages were manually counted in the dorsal fin area (red dashed region). Images are displayed with inverted colour and in black and white for better visualisation. Scale bars= 250 µm. E) Cell proliferation was quantified from confocal images, by counting numbers of EdU positive (+) cells in *Kita* (control) (n= 9), *Kita-RAS* (control for injections) (n= 12) and *Kita-RAS* injected either with MO (n= 8) or CRISPRs (n= 9). F) Maximum projection from confocal images to show cell proliferation in each of the experimental groups. Scale bars= 50 µm. G) Computational analysis was performed on images acquired under a stereomicroscope at 5dpf, and was based on the intensity profile derived from the fluorescence of the identified notochord (red line). Peaks along the notochord (red line) represent the intensity profile. Lesions are identified by higher pixel intensity and broader area under the peak. X and Y axis are displayed in number of pixels and serve as scale bars. H) Violin Plot showing quantification of notochord lesions and rescue of notochord phenotype in *Kita-RAS* (control for injections) (n= 140) and *Kita-RAS* injected either with MO (n= 41) or CRISPRs (n= 105) in comparison with *Kita* (control) (n= 52). Note that MO rescued the notochord phenotype, while CRISPR injections only partially rescued the

notochord. In graphs B), C), E) and H) we used nonparametric, One-way ANOVA, Kruskal-Wallis test, followed by Dunn's multiple comparison test was used, P values are shown when significant ($p<0.05$). B), C) and E) are mean with SD, generated in Prism 8. H) was generated in Python.

Figure 5. Notochord and sheath destabilisation interfere with vertebral column segmentation and mineralisation in *Kita-RAS*. A) Diagram illustrating the expression of *entpd5(+)* in controls. These domains are interspaced by *entpd5(-)*, which will form the IVDs, under normal situation. B) Graph showing numbers of *entpd5+* segments counted from zebrafish at 5dpf and length between 3.8 to 4.1mm. Note slow formation of segments in *Kita-RAS* (n= 24) in comparison with controls (n=25) Unpaired, nonparametric t-test, and Mann-Whitney test were used. Graph shows mean with SD. C) *entpd5* expression in control (*Kita:mCherry*) and *Kita-RAS* at 8dpf. Max projection from z stacks of notochord (*Kita*) and *entpd5:kaeda* are shown for merged channels. Selected regions (dashed box) are shown in higher magnification. Note abnormal expression pattern of *entpd5* (arrows) coinciding with wounded region (dashed arrow). D) Diagram illustrating where the notochord sheath will mineralise from *entpd5+* regions and form the chordacentra (vertebral primordium). E) The length of the first 7 segments of the vertebral column was measured from controls (n= 24 fish) and *Kita-RAS* (n= 23 fish) of similar total length (5 mm ≤ fish length < 6mm) at 14dpf. Graph displays 7 segments and their lengths. Note the high variability in *Kita-RAS*. Unpaired, nonparametric, multiple t-tests were performed for statistical analysis. Line are plotted at mean. P-values are shon when significant ($p<0.05$). F) Alizarin Red and Calcein (bone staining) were used to visualise the mineralised chordacentra at 14dpf in cntrols and *Kita-RAS*. Max projections from confocal images are shown for merged channels. Selected regions (dashed box) are shown in higher magnification. Incomplete mineralisation of the chordacenta (arrows) and ectopic mineralisation towards the IVD domain (arrowhead) were

detected in *Kita-RAS*. All scale bars = 100 µm. G) Alizarin Red was performed in 14dpf fixed samples for measurements of segment lengths. Note uneven mineralisation of the segments. Selected regions (dashed box) are shown in higher magnification. The first 7 vertebral segments are indicated with numbers 1-7. Scale bars = 500 µm.

Figure 6. Transformed notochord cells lead to fusions and vertebral clefts which can be rescued by immune cell modulation. A) µCT images of adult (6 month old, 6mpf) control (*Kita-mCherry*) and *Kita-RAS*. Note severe fusions and shortening of the fish length in *Kita-RAS*. A zoomed region, colour coded for bone mineral density (TMD in $g.cm^3$. HA), is shown as example. Note the decreased mineral density in *Kita-RAS*. Fusions compromising from two (white dashed line, b) to several vertebrae (white dashed line, a) are shown. The arches are also compromised (white dashed arrow). Scale bars = 500 µm. B) TMD calculation. Unpaired two-tailed T-test was used as statistical test (two vertebrae per fish were analysed, control n= 3 fish, *Kita-RAS* n=3 fish). C) Frequency distribution of the length of six consecutive segments, separated by defined IVD space, were measured in Amira using 3D perspective measurement. The studied region is shown with a dashed line and magenta dots in (A). *Kita-RAS* show high variability in length of segments. D) The average of segment length was increased in *Kita-RAS*. Six vertebrae per fish were analysed, control n= 3 fish, *Kita-RAS* n=3 fish. Unpaired, nonparametric T-test (Mann-Whitney test). E) Frequency distribution of fish length in controls and *Kita-RAS* measured in pixels, from X-ray images. F) Fish lengths (measured in pixels) of controls (n= 40) and *Kita-RAS* (n=78). Unpaired, nonparametric T-test (Mann-Whitney test). G) Higher resolution µCT images to show abnormalities in detail. G', fusions of several vertebrae and hemicentra (arrow). G'', lateral view of a hemicentra (arrow). G''', ventral view of hemicentra (arrows). Scale bars = 500 µm. H) One month old (1mpf) control (*Kita-mCherry*) and *Kita:RAS-GFP* stained with Calcein green and Alizarin Red, respectively, to label the bone (magenta). In *Kita-RAS*,

hyperplastic notochord cell is indicated with a white dashed arrow, mineralised IVD with a white arrow and region of incomplete mineralisation and future cleft is marked with a dashed line. Note that notochordal cells fail to organise in IVD domains. Scale bars = 50 µm. I) 1mpf control and *Kita:RAS-G*FP showing osteoblasts (Tg(*osx:NTR-mCherry*)). Arrows indicate regions of increased osteoblasts, dashed arrows show regions lacking osteoblasts and abnormal growth of arches. Pictures were processed to show pixel intensity (blue = low intensity), to visualise where osteoblasts are highly expressed. Two vertebrae in each fish were selected for quantification of mean pixel intensity. J) Alizarin red staining of 1mpf *Kita, Kita-RAS* and *Kita-RAS+CRISPR.* Note an intermediate (less severe) phenotype in *Kita-RAS+CRISPR* suggesting rescue of bone phenotype. K) Violin plot to show the distribution of vertebral column severity scores, from 0 (less severe) to 3 (most severe), in *Kita* (n=47), *Kita-RAS* (n= 44) and *Kita-RAS+CRISPR* (n= 83). One-Way ANOVA and Tukey's multiple comparisons test were used, p values are indicated when significant. Scale bars = 50 µm.

Figure 7. Fibrotic nucleus pulposus and abnormal annulus fibrosus in *Kita-RAS* resemble intervertebral disc degeneration. A) Schematic of a histological section of the vertebral column of zebrafish (off from the midline) showing two consecutive IVDs. IVD = intervertebral disc; NP = nucleus pulposus; AF = annulus fibrosus; co = collagen layers; el = elastin layer; b = bone; ns = notochord sheath. B) Histological sections of adult control (*Kita-mCherry*) and *Kita-RAS* fish stained for Toluidine Blue (morphology), AFOG (fibrosis), and Picro-sirius red (fibrosis and collagen fibre thickness). Bone (b) and inner nucleus pulposus (NP) are indicated on the control Toluidine Blue picture. Abnormal fibrosis (black, orange and white arrows), cellularity and disorganisation of the NP were detected in *Kita-RAS* fish. The regions within the dashed box (Picro-sirius red staining) are shown at higher magnification to show the bone in detail. Asterisks were added to help with orientation, and they show the same position in lower and higher magnification pictures. Poor quality of bone

can be measured by the tons of colours from Picro-sirius red staining. Thicker fibres are red and thinner fibres are blue/green (colour bar). C) Collagen fibre quantification was performed by determining the means of pixel colours (red, green and blue) in the Picro-sirius red staining pictures. Note a reduction of thick (red) and very thin (blue) fibres in *Kita-RAS* (n=9 vertebrae, n= 3 fish) in comparison to controls (n= 6 vertebrae, n= 3 fish). Unpaired, nonparametric t-test, and Mann-Whitney test were used. Graphs show mean with SD, p values are indicated when significant ($p<0.05$). D) Toluidine blue staining to show details of the AF area in control (*Kita-mCherry*) and *Kita-RAS*. Note the loss of the layers of collagen and elastin in *Kita-RAS* and disorganised and higher number of osteoblasts (arrow). Internal collagen layer is mixed with abnormal cells (dashed arrow). All scale bars = 50 µm.

Figure 8. Pre-neoplastic notochord cells drive abnormal vertebral column development and interfere with bone homeostasis in zebrafish.

In wild-type zebrafish, the notochord is formed by a notochord sheath epithelium (nse) wrapping notochord vacuolated cells (nvc) (A). Innate immune cells, in particular neutrophils (n) and macrophages (m), are not directed to the notochord and they do not trespass the ns (B). The segmentation of the notochord to form the future vertebrae and IVDs starts with differentiation of notochord sheath cells to express *entpd5* in interspaced domains (C). These segments will mineralise (chordacentra) and originate individual vertebra while inter-segment regions will form the IVDs (D). Osteoblasts (ob) and osteoclasts (oc) are evenly distributed in the centra and arches (E). When RAS is expressed in the notochord cells, transformed vacuolated cells collapse and a fibrous “scar” tissue is formed (A’). The notochord sheath layer is destabilised, triggering a prolonged recruitment of neutrophils and macrophages (B’). The notochord sheath cells fail to differentiate and to express *entpd5* in specific domains, showing a delay and abnormal pattern of expression (C’). This leads to abnormal chordacentra formation (D’), consequently leading to fusions, clefts and abnormalities in the

adult vertebral column (E'). IVDs are lost due to fusions. Osteoblasts and osteoclasts are distributed disorderly in centra and arches and in higher numbers (E'). Moreover, pre-neoplastic cells continue to adult leading to nucleus pulposus abnormalities and poor bone quality. Chordoma development and bone phenotype can be controlled by immunomodulation of neutrophils and macrophages.

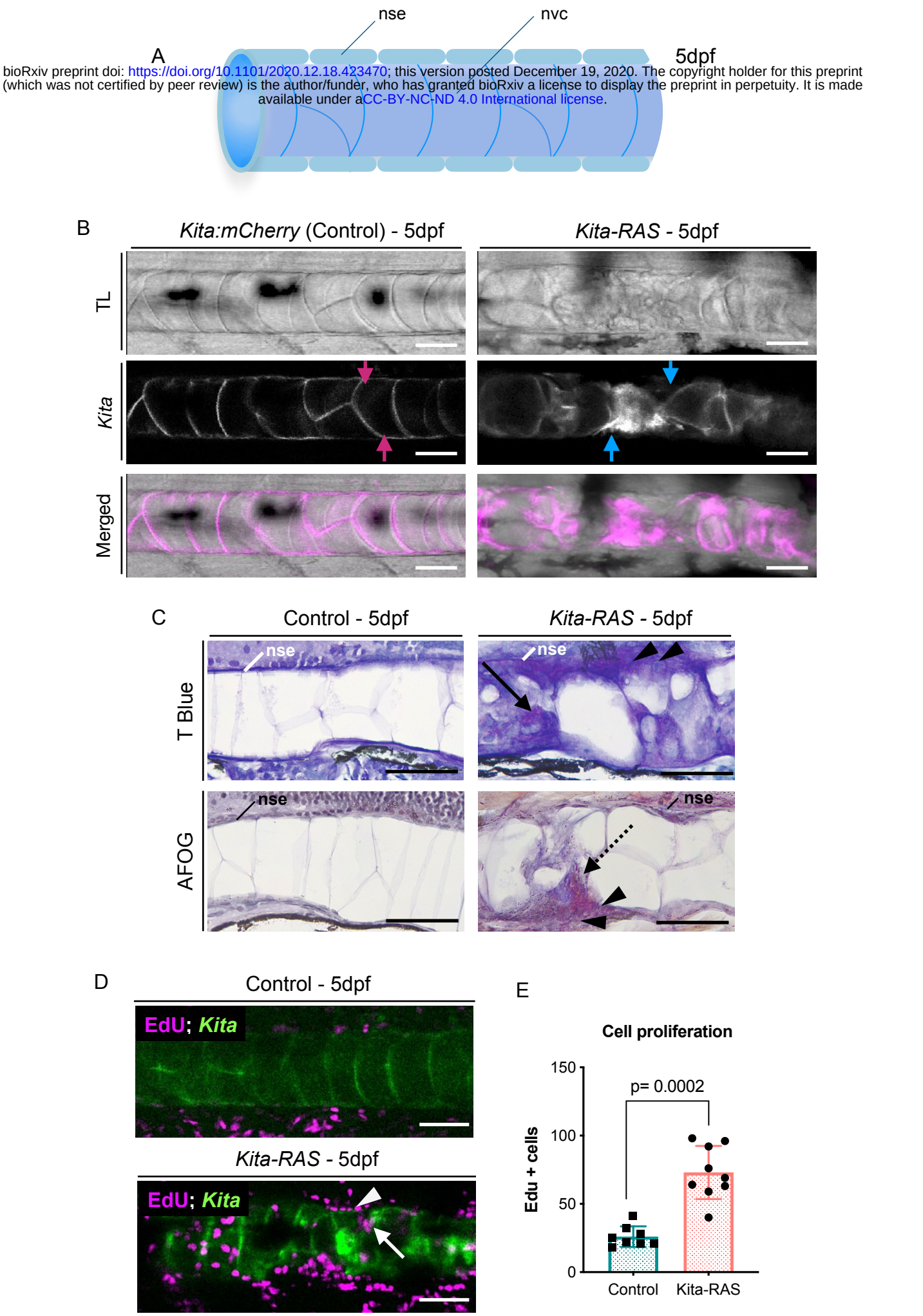

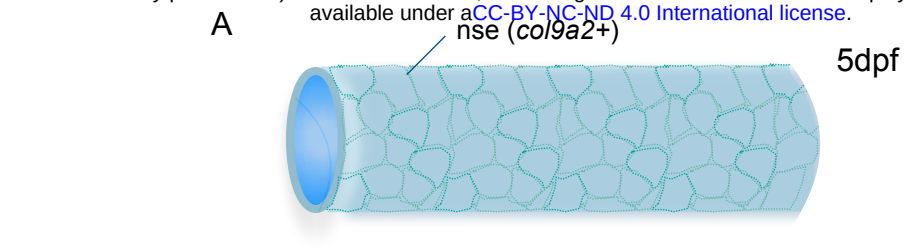

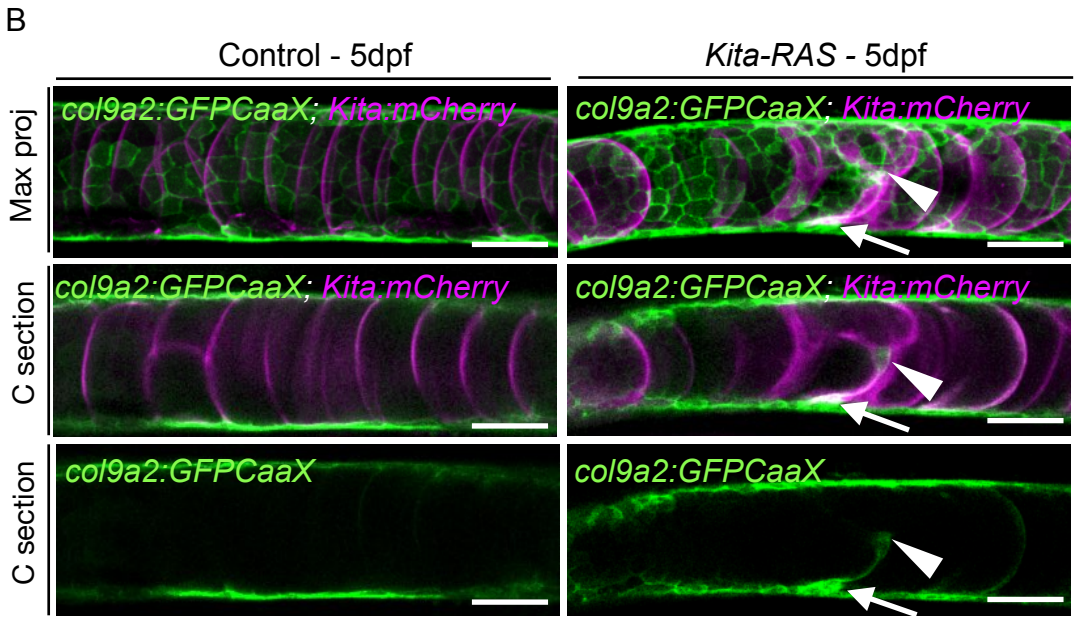

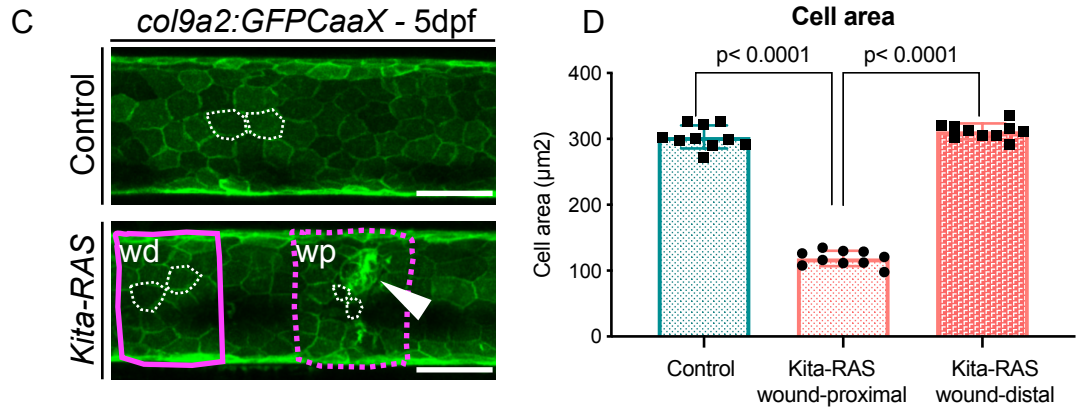

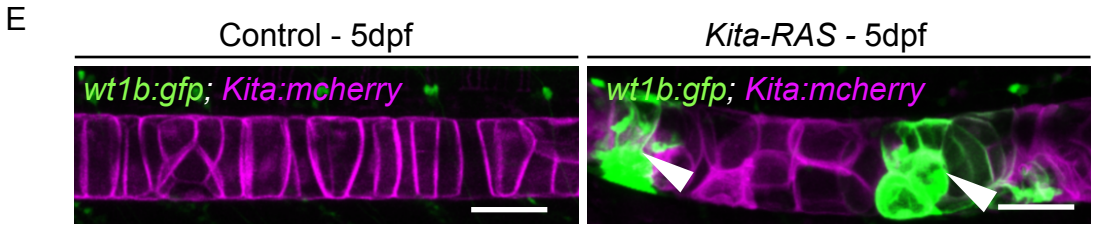

A

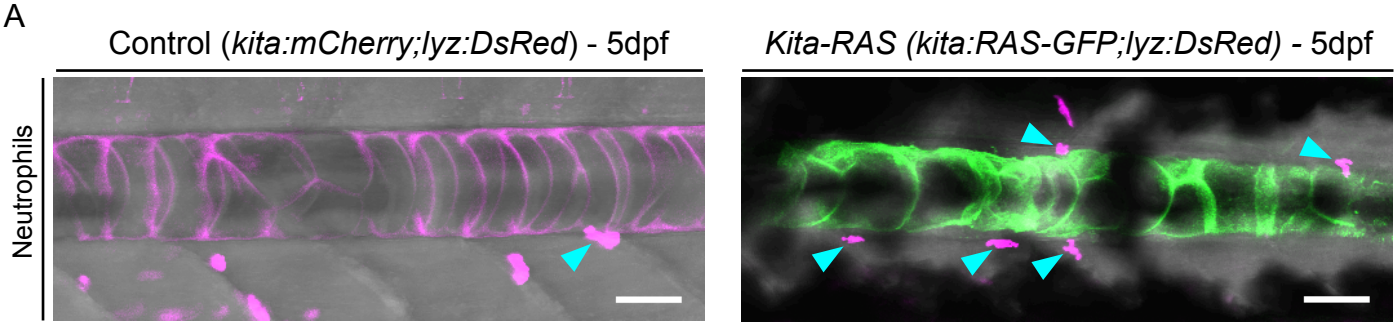
Control (kita:mCherry;lyz:DsRed) - 5dpf
Kita-RAS (kita:RAS-GFP;lyz:DsRed) - 5dpf
Neutrophils

B

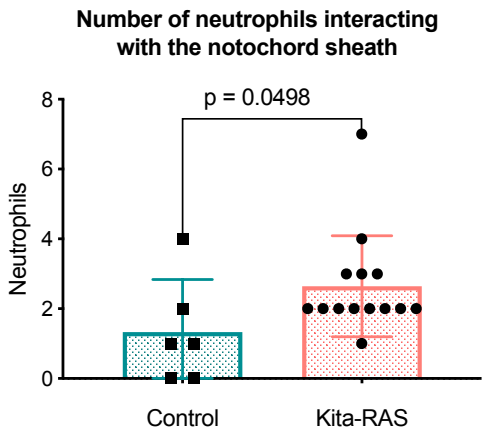
Number of neutrophils interacting with the notochord sheath
p = 0.0498
Neutrophils
0
2
4
6
8
Control
Kita-RAS

C

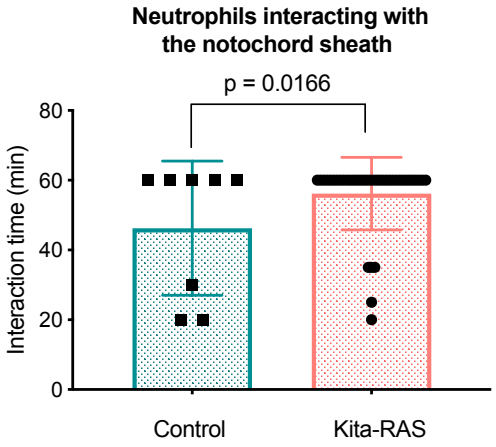
Neutrophils interacting with the notochord sheath
p = 0.0166
Interaction time (min)
0
20
40
60
80
Control
Kita-RAS

D

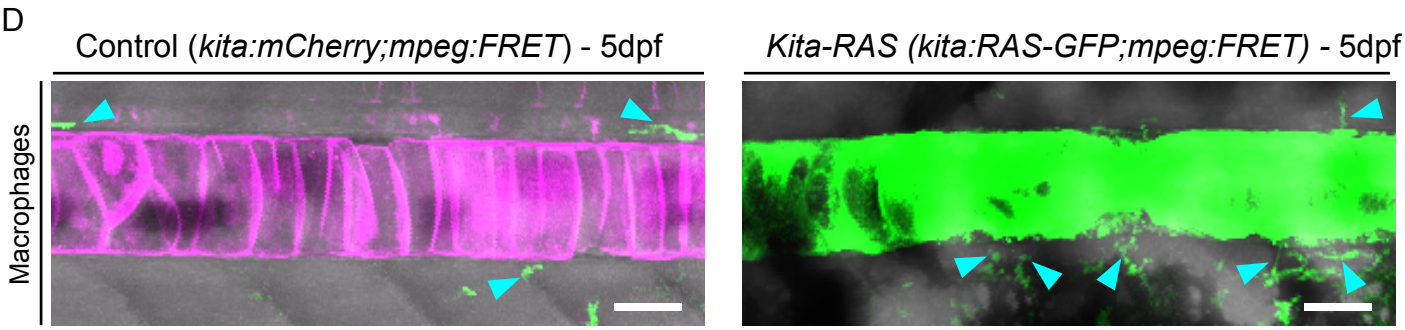
Control (kita:mCherry;mpeg:FRET) - 5dpf
Kita-RAS (kita:RAS-GFP;mpeg:FRET) - 5dpf
Macrophages

E

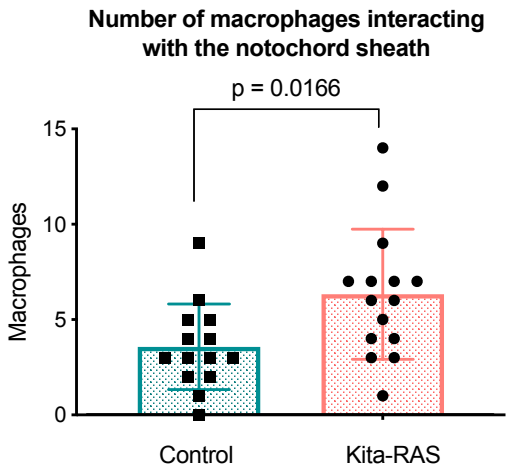
Number of macrophages interacting with the notochord sheath
p = 0.0166
Macrophages
0
5
10
15
Control
Kita-RAS

F

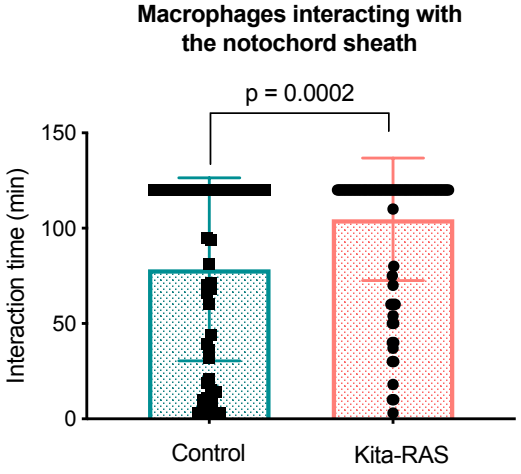
Macrophages interacting with the notochord sheath
p = 0.0002
Interaction time (min)
0
50
100
150
Control
Kita-RAS

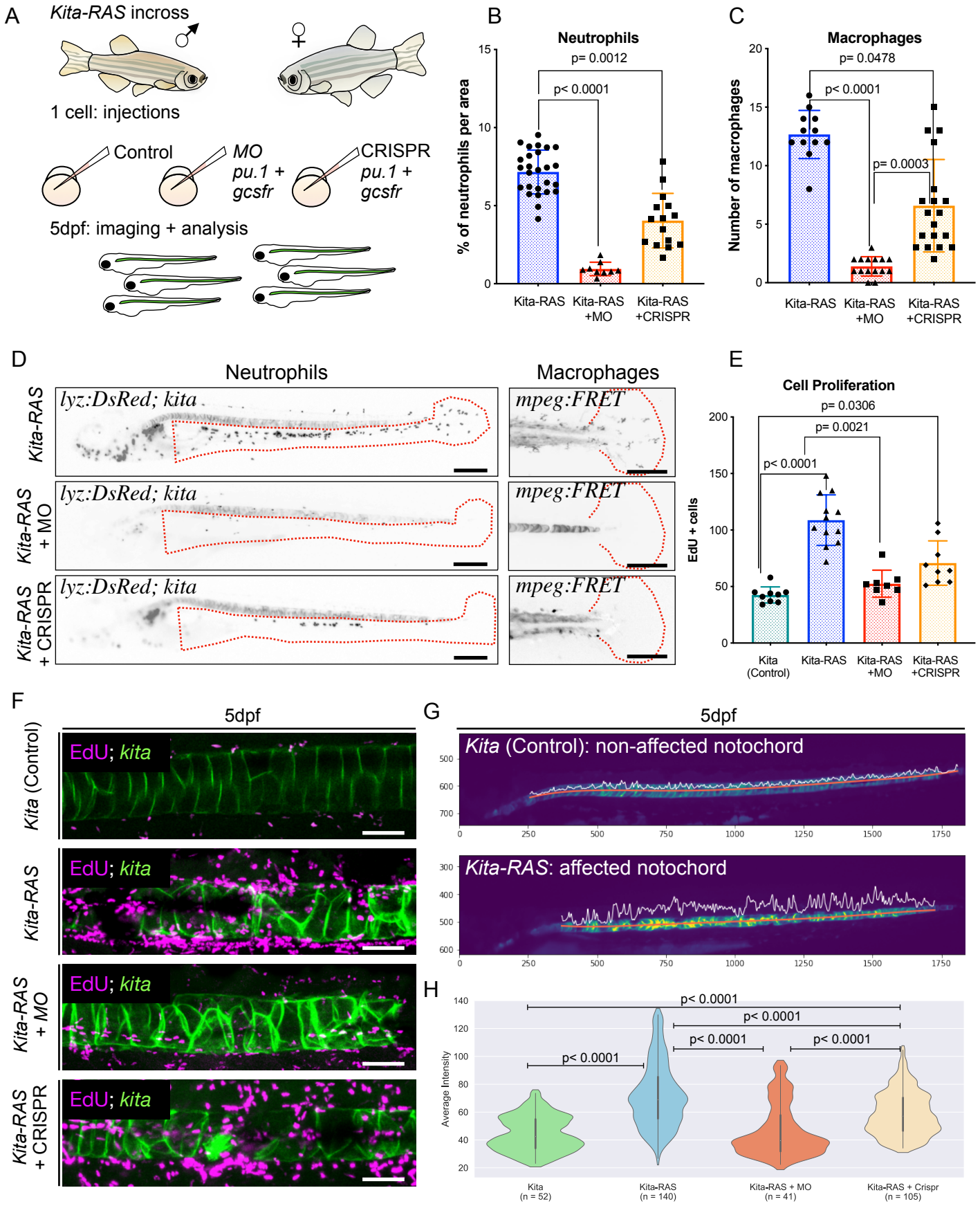
A
Kita-RAS incross
1 cell: injections
Control
MO pu.1 + gcsfr
CRISPR pu.1 + gcsfr
5dpf: imaging + analysis
B
Neutrophils
p= 0.0012
p< 0.0001
% of neutrophils per area
Kita-RAS
Kita-RAS +MO
Kita-RAS +CRISPR
C
Macrophages
p= 0.0478
p< 0.0001
p= 0.0003
Number of macrophages
D
Neutrophils
Macrophages
Kita-RAS
Kita-RAS + MO
Kita-RAS + CRISPR
lyz:DsRed; kita
mpeg:FRET
E
Cell Proliferation
p= 0.0306
p= 0.0021
p< 0.0001
EdU + cells
Kita (Control)
F
5dpf
Kita (Control)
Kita-RAS
Kita-RAS + MO
Kita-RAS + CRISPR
EdU; kita
G
5dpf
Kita (Control): non-affected notochord
Kita-RAS: affected notochord
H
p< 0.0001
Average Intensity
Kita (n = 52)
Kita-RAS (n = 140)
Kita-RAS + MO (n = 41)
Kita-RAS + Crispr (n = 105)

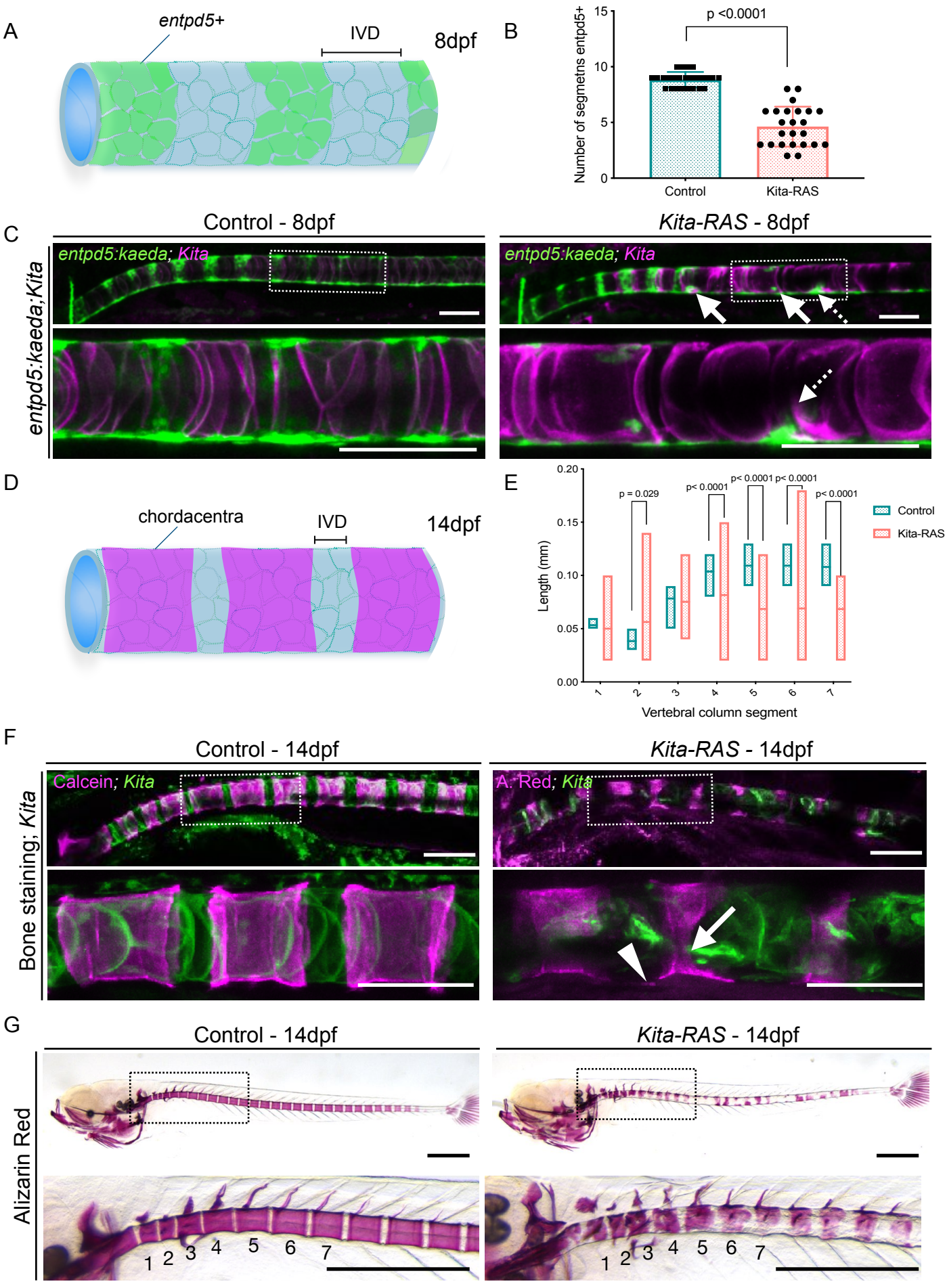
A
entpd5+
IVD
8dpf
B
p <0.0001
Number of segmetns entpd5+
15
10
5
0
Control
Kita-RAS
C
Control - 8dpf
Kita-RAS - 8dpf
entpd5:kaeda;Kita
entpd5:kaeda; Kita
entpd5:kaeda; Kita
D
chordacentra
IVD
14dpf
E
p = 0.029
p< 0.0001
p< 0.0001
p< 0.0001
p< 0.0001
Length (mm)
0.20
0.15
0.10
0.05
0.00
1
2
3
4
5
6
7
Vertebral column segment
Control
Kita-RAS
F
Control - 14dpf
Kita-RAS - 14dpf
Bone staining; Kita
Calcein; Kita
A. Red; Kita
G
Control - 14dpf
Kita-RAS - 14dpf
Alizarin Red
1 2 3 4 5 6 7
1 2 3 4 5 6 7

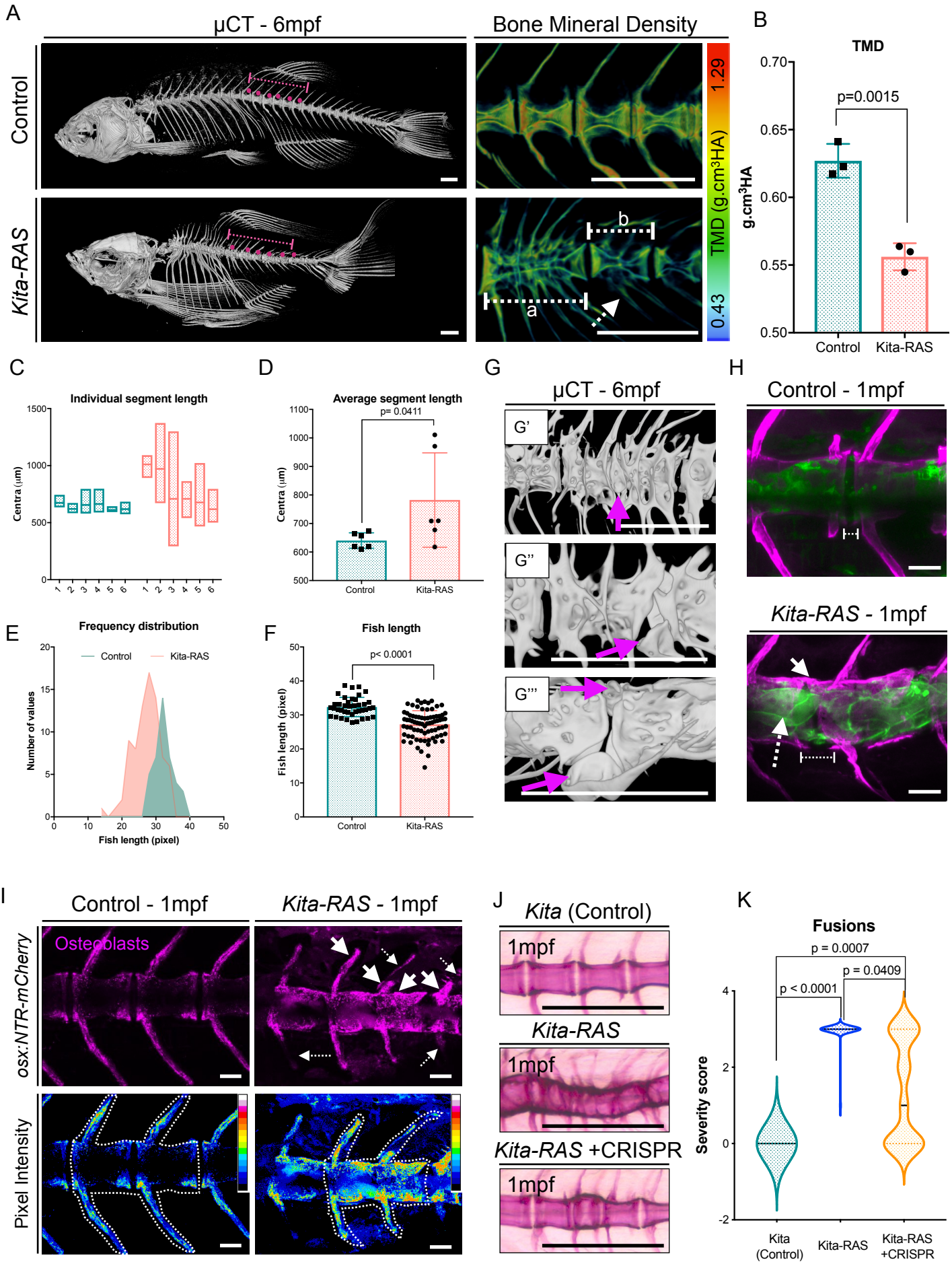
A
µCT - 6mpf
Bone Mineral Density
Control
Kita-RAS
b
a
1.29
TMD (g.cm³HA)
0.43
B
TMD
p=0.0015
g.cm³HA
0.70
0.65
0.60
0.55
0.50
Control
Kita-RAS
C
Individual segment length
Centra (µm)
1500
1000
500
0
D
Average segment length
p= 0.0411
Centra (µm)
1100
1000
900
800
700
600
500
Control
Kita-RAS
E
Frequency distribution
Control
Kita-RAS
Number of values
20
15
10
5
0
0
10
20
30
40
50
Fish length (pixel)
F
Fish length
p< 0.0001
Fish length (pixel)
50
40
30
20
10
0
Control
Kita-RAS
G
µCT - 6mpf
G'
G''
G'''
H
Control - 1mpf
Kita-RAS - 1mpf
I
Control - 1mpf
Kita-RAS - 1mpf
osx:NTR-mCherry
Osteoblasts
Pixel Intensity
J
Kita (Control)
1mpf
Kita-RAS
1mpf
Kita-RAS +CRISPR
1mpf
K
Fusions
p = 0.0007
p = 0.0409
p < 0.0001
Severity score
4
2
0
-2
Kita (Control)
Kita-RAS
Kita-RAS +CRISPR

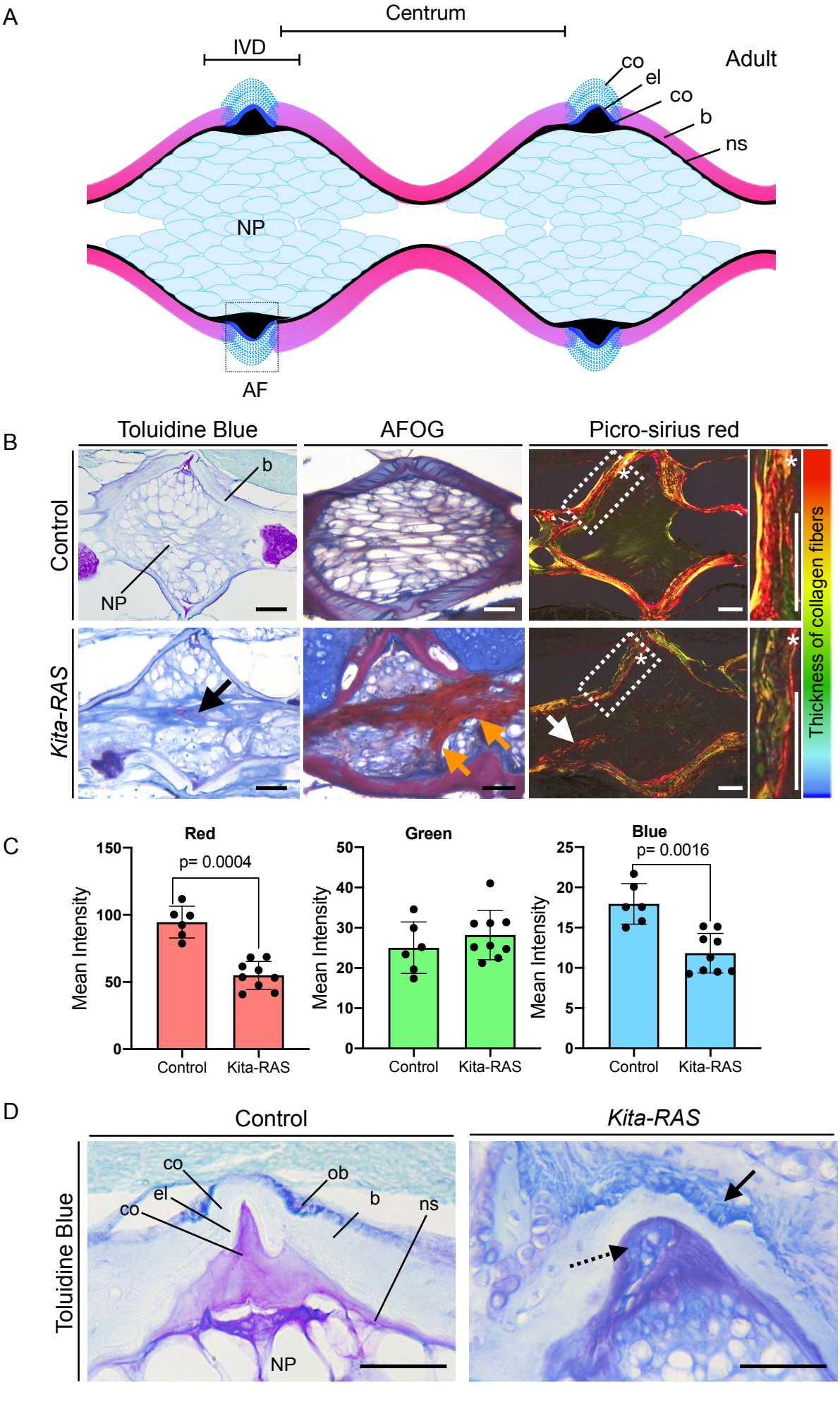
A
Centrum
IVD
Adult
co
el
co
b
ns
NP
AF
B
Toluidine Blue
AFOG
Picro-sirius red
Control
Kita-RAS
b
NP
Thickness of collagen fibers
C
Red
Green
Blue
p= 0.0004
p= 0.0016
Mean Intensity
Control
Kita-RAS
D
Control
Kita-RAS
Toluidine Blue
co
el
co
ob
b
ns
NP

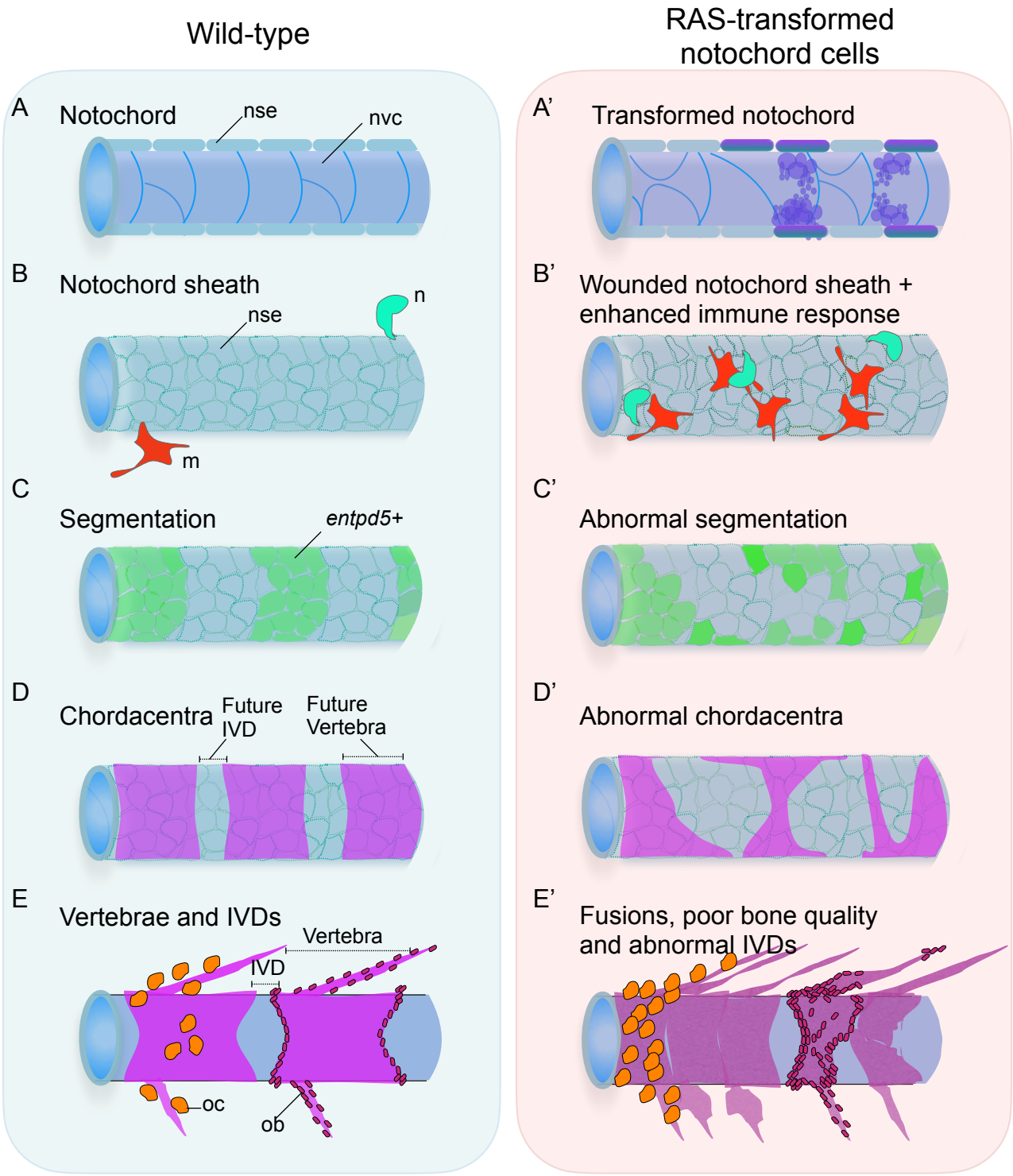
Wild-type
RAS-transformed notochord cells
A
Notochord
nse
nvc
A'
Transformed notochord
B
Notochord sheath
n
nse
m
B'
Wounded notochord sheath + enhanced immune response
C
Segmentation
entpd5+
C'
Abnormal segmentation
D
Chordacentra
Future IVD
Future Vertebra
D'
Abnormal chordacentra
E
Vertebrae and IVDs
Vertebra
IVD
oc
ob
E'
Fusions, poor bone quality and abnormal IVDs